

Floquet scars and prethermal fragmentation in a driven spin-one chain

Krishanu Ghosh¹, Diptiman Sen², and K. Sengupta¹

¹*School of Physical Sciences, Indian Association for the Cultivation of Science, Kolkata 700032, India.*

²*Center for High Energy Physics, Indian Institute of Science, Bengaluru 560094, India.*

(Dated: March 9, 2026)

We study the periodic dynamics of a spin-one chain driven using a square-pulse protocol with amplitude Q_0 and frequency ω_D . The Hamiltonian of the spin chain hosts a thermodynamically large number of Z_2 -valued conserved quantities W_ℓ on the links ℓ . This allows us to study the Floquet dynamics of this chain within a given sector with fixed values of W_ℓ . For the sector with all $W_\ell = 1$, we find signatures of quantum many-body scar states for $\hbar\omega_D \gg Q_0$; they lead to oscillatory dynamics and fidelity revival for specific initial states. Upon lowering ω_D , we find an ergodic regime exhibiting fast thermalization consistent with the prediction of the (Floquet) eigenstate thermalization hypothesis. In addition, we identify special drive frequencies $\omega_n^* = Q_0/(2n\hbar)$ (where $n = 1, 2, 3, \dots$) at which the Floquet Hamiltonian exhibits prethermal strong Hilbert space fragmentation (HSF) with the largest fragment being ergodic; in contrast, a weak HSF is found at $\omega'_n = Q_0/[\hbar(2n+1)]$ (where $n = 0, 1, 2, \dots$). We also study the sector with $W_\ell = \{\dots 1, 1, -1, 1, 1, -1 \dots\}$ which shows strong HSF at ω_n^* but no fragmentation at ω'_n . Our analysis indicates that the strong HSF in this sector harbors an integrable largest fragment. We provide numerical support for our analytical and perturbative results using exact-diagonalization (ED) studies on finite chains of length $L \leq 24$. Our numerical results for entanglement entropy, fidelity, and correlation functions of the driven chain provide definitive signatures of prethermal strong HSF for both sectors.

I. INTRODUCTION

The non-equilibrium dynamics of closed quantum systems have been intensely studied in recent years [1–17]. Such studies have received support from experiments carried out with ultracold atoms in optical lattices [13, 14, 18–24]. Recently, research in this area has focused on periodically driven systems. This is primarily due to the fact that such systems exhibit several phenomena that have no analogs in their aperiodically driven counterparts. Some examples of such phenomena include dynamical localization [25–31] and transition [32–39], dynamical freezing [40–46], prethermal time crystalline behavior [47–56], generation of Floquet states with non-trivial topology [57–65], prethermal realization of quantum scars [66–73], Hilbert space fragmentation (HSF) [74–84] and Meissner phases [85]. In addition, it has led to ways of reducing the heating in driven quantum systems [86–88].

The time-evolution of a periodically driven system is controlled by its evolution operator $U(t, 0)$. At stroboscopic times $t = mT$, where $T = 2\pi/\omega_D$ is the time period of the drive, $m \in Z$ is the number of drive cycles, and ω_D is the drive frequency, these operators are described by a Floquet Hamiltonian H_F through the relation $U(mT, 0) = \exp[-iH_F mT/\hbar]$, where \hbar denotes Planck's constant. The exact computation of H_F is usually difficult; for most system, one resorts to perturbative methods where the inverse of the drive amplitude or drive frequency is treated as the perturbation parameter [10, 12]. These methods are therefore useful in the large drive frequency or amplitude regime where the Floquet Hamiltonian resembles Hamiltonians with short-range interactions. In these regimes, the driven systems usually hosts a long prethermal timescale before eventual

thermalization[89–95]; the dynamics within this regime is typically controlled by the first term, $H_F^{(1)}$, of the perturbation series. It has been shown that $H_F^{(1)}$ may host additional emergent symmetries which control the dynamics in this prethermal regime; such emergent symmetries are key to understanding several properties of such driven systems [17].

In this work, we shall study the dynamics of a periodically driven spin chain. The Hamiltonian of the spin chain, shown schematically in the bottom panel of Fig. 1, is given by $H = H_0 + H_1$, where

$$H_0 = J \sum_j S_j^x S_{j+1}^y, \quad H_1 = Q \sum_j (S_j^x S_{j+1}^y)^2, \quad (1)$$

where S_j^α denotes spin-one SU(2) matrices on site j of the chain [96–98]. We note at the outset that the Hamiltonian in Eq. 1 is equivalent to a spin-one Kitaev chain (shown schematically in the top panel of Fig. 1) studied in Refs. 96 and 97 via an unitary transformation of the spins $S_{2j}^x = S_{2j}^y$, $S_{2j}^y = S_{2j}^x$, and $S_{2j}^z = -S_{2j}^z$ on all the even sites of the chain. In what follows, we will drive H_1 according to a square pulse protocol given by

$$Q(t) = -Q_0 \quad \text{for } t \leq T/2 \\ = Q_0 \quad \text{for } T/2 < t \leq T, \quad (2)$$

in the large drive amplitude regime $Q_0 \gg J$. Our numerical study of this model will be facilitated by the fact that the model given by Eq. 1 is known to host a large number of Z_2 -valued conserved quantities W_ℓ which live on a link ℓ separating sites j and $j+1$. These are given by

$$W_\ell = \Sigma_j^y \Sigma_{j+1}^x, \quad \Sigma_j^\alpha = e^{i\pi S_j^\alpha}, \quad (3)$$

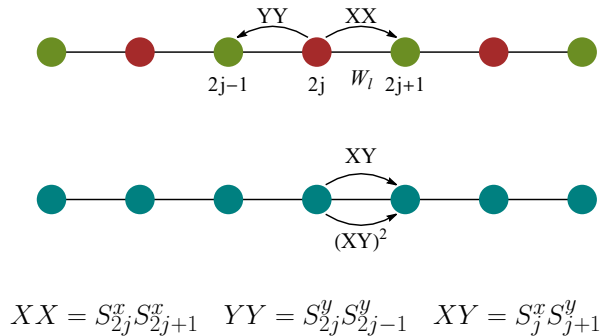


FIG. 1. Schematic representation of the spin-one Kitaev chain. The top panel shows the representation in terms of $S_{2j}^x S_{2j+1}^x$ and $S_{2j}^y S_{2j-1}^y$ for even site $2j$ (shown as XX and YY respectively). For each of the links ℓ between any two sites, W_ℓ , defined in Eq. 3 of the main text, is conserved. The bottom panel shows an equivalent representation in terms of $XY \equiv S_j^x S_{j+1}^y$ on all sites of the chain; these two Hamiltonians are unitarily related as discussed in the text. An interaction term of the form $(XY)^2$ is also added; together they form the Hamiltonian H studied in the text.

where $\alpha = x, y, z$. The existence of the W_ℓ 's enables one to study the dynamics of the model within a given sector allowing for exact diagonalization (ED) of the spin chain of length $L \leq 24$. In what follows we shall study the dynamics of the driven spin chain for two sectors; the first of these has $W_\ell = 1$ for all links while the second has a periodic pattern given by $W_\ell = \{\dots 1, 1, -1, 1, 1, -1 \dots\}$. Our numerical results will be supported by analytical, albeit perturbative, computations of the Floquet Hamiltonian in the large drive amplitude regime using Floquet perturbation theory (FPT) [12].

The central results that we obtain from our studies are as follows. First we obtain an analytic expression for the first-order Floquet Hamiltonian $H_F^{(1)}$ in the strong drive amplitude regime. Our analysis indicates that $H_F^{(1)} \simeq H_0$ in the large drive frequency regime ($\hbar\omega_D \gg Q_0$). The system hosts quantum many-body scars in this regime which is expected to lead to oscillatory dynamical behavior for a class of initial states. Upon lowering the drive frequency, $H_F^{(1)}$ deviates from H_0 and the scar induced oscillatory dynamics is replaced by fast thermalization consistent with Floquet ETH.

Second, our analysis shows the existence of special drive frequencies $\omega_m^* = Q_0/(2n\hbar)$ ($n \in \mathbb{Z}$) at which the driven system exhibits prethermal HSF [77–82] for the sectors with all $W_\ell = 1$ and $W_\ell = \{\dots 1, 1, -1 \dots\}$. We provide explicit analytic counting for such HSF by identifying and counting the number of states in the largest fragment of $H_F^{(1)}$ at these frequencies via transfer matrix methods. Our analysis shows that the largest fragment is ergodic in the sector with all $W_\ell = 1$; in contrast, it is integrable for the $W_\ell = \{\dots 1, 1, -1 \dots\}$ sector.

Third, we find that for $\omega_D = \omega'_n = Q_0/[\hbar(2n + 1)]$ ($n \in \mathbb{Z}$), $H_F^{(1)}$ the driven chain exhibits weak prethermal fragmentation for $W_\ell = 1$ sector. We numerically find that at these drive frequencies, the Hilbert space of $H_F^{(1)}$ supports dynamically disconnected fragments in the Fock basis. However, the number of such fragments does not grow exponentially with system size L ; rather it grows only linearly with L . We note that the possibility of such different prethermal behaviors for different drive frequencies has been envisaged in Ref. 81; our model provides a concrete realization of this phenomenon. In contrast, the $W_\ell = \{\dots 1, 1, -1 \dots\}$ sector does not exhibit any fragmentation for $\omega_D = \omega'_n$.

Fourth, we carry out exact numerical studies of quantum dynamics of the model using ED for both sectors. We compute the entanglement entropy S , the fidelity $\mathcal{F}(mT) = |\langle \psi_{\text{initial}} | \psi(mT) \rangle|$ (where m is the number of drive cycles), and the correlation function $C_{j,j+n} = \langle \psi(mT) | \hat{O}_j \hat{O}_{j+n} | \psi(mT) \rangle \equiv C_0$, where $\hat{O}_j = (S_j^x S_{j+1}^y)^2$, for the driven chain as a function of m at different drive frequencies. Our numerical results confirm the existence of quantum scars leading to oscillatory behaviors of \mathcal{F} and C_0 at large drive frequencies for both sectors. Moreover, upon lowering ω_D , these quantities exhibit rapid thermalization consistent with ETH. We also find distinct behaviors of the entropy, the fidelity, and the correlation function at $\omega_D = \omega_1^*$ and ω'_1 as discussed below.

For the sector with all $W_\ell = 1$, the entanglement entropy of initial Fock states chosen randomly from the Hilbert space saturates to different Page values at $\omega_D = \omega_1^*$. This behavior is indicative of the presence of dynamically disconnected fragments in the Hilbert space. Moreover, for a chosen initial frozen state, S remains pinned to its initial value S_0 for a large number of cycles; thus the deviation from S from S_0 allows us to estimate the prethermal timescale up to which $H_F^{(1)}$ controls the dynamics. Our numerics indicates that the extent of this regime grows exponentially with the drive amplitude Q_0 which is consistent with the results of Refs. [77]. For the $W_\ell = \{\dots 1, 1, -1 \dots\}$ sector, we find that for an initial state chosen from the largest fragment, the entanglement entropy exhibits oscillatory behavior between $S = 0$ and $\ln 2$ which is consistent with the integrable nature of the largest fragment. We also find a distinct behavior of S for the sector with all $W_\ell = 1$ at $\omega_D = \omega'_1$. For this frequency, for several randomly chosen initial Fock states, S/S_p saturates to a few distinct values at large times; this is consistent with the presence of weak thermalization.

The behavior of \mathcal{F} also indicates the presence of such HSF at special frequencies. For the sector with all $W_\ell = 1$ sector, for an initial state $|\psi_{\text{initial}}\rangle$ chosen from the largest fragment, we find that the fluctuations of \mathcal{F} at large times increase at $\omega_D = \omega_1^*$ indicating a much stronger finite-size effect; this arises due to the reduced Hilbert space dimension (HSD) of individual fragments. In contrast, for an initial state from the largest fragment in the $W_\ell = \{\dots 1, 1, -1 \dots\}$ sector, \mathcal{F} shows an oscillatory

behavior with perfect revivals for a long time indicating integrability of the fragment. Moreover, for an initial frozen state in this sector, \mathcal{F} remains close to unity for a large number of cycles followed by a slow relaxation to its thermal value. The latter behavior occurs due to the presence of higher order terms in the Floquet Hamiltonian which do not host HSF.

The characteristics of the driven system portrayed by S and \mathcal{F} receives further support from the behavior of C_0 . In the $W_\ell = 1$ sector, starting from the initial Fock state $|\psi_1\rangle = |\cdots xyxy \cdots\rangle$, C_0 shows scar-induced oscillations for large drive frequencies, followed by fast thermalization as the frequency is lowered. In contrast, at $\omega_D = \omega_1^*$, C_0 remains pinned to its initial value for $m \leq 200$ which is consistent with the behavior of the dynamics starting from a frozen state. A similar behavior is also found for the $W_\ell = \{\cdots 1, 1, -1 \cdots\}$ sector for the initial state $|\psi'_1\rangle = |\cdots x, y, x, x, y, x, \dots\rangle$.

The plan of the rest of the paper is as follows. In Sec. II, we chart out several properties of the Hamiltonian H and provide an analytic computation of the HSDs of its different sectors using a transfer matrix method. This is followed by Sec. III, where we present an analytic computation of the first-order Floquet Hamiltonian $H_F^{(1)}$ for large Q_0/J using Floquet perturbation theory (FPT) for both sectors; we also provide analytical and numerical estimates of the number of fragments and the HSD of the largest fragments of $H_F^{(1)}$ at $\omega_D = \omega_n^*$ and ω'_n . Next, in Sec. IV, we provide exact numerical results for S , \mathcal{F} and C_0 using ED. Finally, we discuss our main results and conclude in Sec. V.

II. MODEL HAMILTONIAN AND ITS SECTORS

In this section, we will chart out some basic properties of the spin chain. The analysis of the Hamiltonian and the presence of different dynamically disconnected sectors is discussed in Sec. II A whereas the computation of dimension of these sectors, using a transfer matrix approach, is presented in Sec. II B.

A. Properties of the Hamiltonian

The Hamiltonian of the spin-one chain is given by Eq. 1. In what follows, we will work with the representation [98]

$$(S^\alpha)_{\beta\gamma} = i\epsilon_{\alpha\beta\gamma}, \quad (4)$$

where $\epsilon_{\alpha\beta\gamma}$ is the Levi-Civita antisymmetric tensor. We note that in the representation given by Eq. 4, the matrices Σ_j^α (Eq. 3) are diagonal and are given by

$$\begin{aligned} \Sigma_j^x &= \text{Diag}[1, -1, 1], & \Sigma_j^y &= \text{Diag}[-1, 1, -1], \\ \Sigma_j^z &= \text{Diag}[-1, -1, 1]. \end{aligned} \quad (5)$$

It is easy to see that $\Sigma_j^x \Sigma_j^y \Sigma_j^z = I$, where I is the 3×3 identity matrix for all j ; moreover, they satisfy $[H, \Sigma_j^x \Sigma_{j+1}^y] = 0$ implying that $W_\ell = \pm 1$ are Z_2 -valued conserved quantities. This leads to an exponentially large number of dynamically disconnected sectors characterized by specific values of W_ℓ on each link [96–98]. In what follows we shall study the properties of H in two sectors corresponding to all $W_\ell = 1$ and $W_\ell = \{\cdots 1, 1, -1 \cdots\}$. The former sector has the largest HSD and hosts the ground state of the model while the latter hosts the first excited state. The dimensions of these sectors will be analyzed in the next subsection.

The local basis vectors on any site j which can be used to construct the Fock states of the model can be written as

$$|x_j\rangle = \begin{pmatrix} 1 \\ 0 \\ 0 \end{pmatrix}, \quad |y_j\rangle = \begin{pmatrix} 0 \\ 1 \\ 0 \end{pmatrix}, \quad |z_j\rangle = \begin{pmatrix} 0 \\ 0 \\ 1 \end{pmatrix}. \quad (6)$$

The corresponding Fock states can be labeled as $|\cdots \alpha_{j-1} \beta_j \gamma_{j+1} \delta_{j+2} \cdots\rangle$, where $\alpha, \beta, \gamma, \delta$ take values x, y , or z . The advantage of this construction becomes apparent upon noticing that on any site j ,

$$\begin{aligned} S_j^\alpha |\beta_j\rangle &= -i\epsilon_{\alpha\beta\gamma} |\gamma_j\rangle, \\ (S_j^\alpha)^2 |\beta_j\rangle &= (1 - \delta_{\alpha\beta}) |\beta_j\rangle, \quad \Sigma_j^\alpha = 1 - 2(S_j^\alpha)^2 \end{aligned} \quad (7)$$

so that the Fock states constructed out of these basis vectors are eigenstates of H_1 .

The construction of these basis vector also allows us to efficiently chart out the states in a given sector. For example, to have $W_\ell = \pm 1$ on any link ℓ separating the sites j and $j+1$, we need the spin states on sites j and $j+1$ to satisfy $\Sigma_j^y \Sigma_{j+1}^x |\alpha_j \beta_{j+1}\rangle = \pm 1$, where α and β can take values x, y, z . A straightforward calculation shows that $W_\ell = 1$ corresponds to the states with configurations

$$|x_j y_{j+1}\rangle, |y_j x_{j+1}\rangle, |z_j z_{j+1}\rangle, |z_j y_{j+1}\rangle, |x_j z_{j+1}\rangle, \quad (8)$$

while that for $W_\ell = -1$ they correspond to

$$|x_j x_{j+1}\rangle, |y_j y_{j+1}\rangle, |y_j z_{j+1}\rangle, |z_j x_{j+1}\rangle. \quad (9)$$

This allows us to construct the many-body Fock states in different sectors efficiently; any such Fock state $|p\rangle$ satisfies

$$H_1 |p\rangle = \epsilon_p |p\rangle, \quad (10)$$

where $\epsilon_p = Qp$, and the value of the integer p depends on the specific configuration of the basis vectors used to construct $|p\rangle$. We note that $|p\rangle$ represents degenerate states since multiple configurations involving different basis vectors at different sites can lead to the same ϵ_p .

Finally, we note that the action of H_0 and H_1 on these states can be charted out in a straightforward manner. For states corresponding to $W_\ell = 1$, we find that

$$\begin{aligned} H_1 |x_j y_{j+1}\rangle &= H_1 |z_j y_{j+1}\rangle = H_1 |x_j z_{j+1}\rangle = 0, \\ H_1 |y_j x_{j+1}\rangle &= Q |y_j x_{j+1}\rangle, \quad H_1 |z_j z_{j+1}\rangle = Q |z_j z_{j+1}\rangle, \end{aligned} \quad (11)$$

while for the states in the $W_\ell = -1$ sector, one has

$$\begin{aligned} H_1|x_j x_{j+1}\rangle &= H_1|y_j y_{j+1}\rangle = 0, \\ H_1|z_j x_{j+1}\rangle &= Q|z_j z_{j+1}\rangle, \quad H_1|y_j z_{j+1}\rangle = Q|y_j z_{j+1}\rangle. \end{aligned} \quad (12)$$

The action of H_0 on these states can also be obtained in an analogous manner. For states in the $W_\ell = +1$ sector, we find that

$$\begin{aligned} H_0|x_j y_{j+1}\rangle &= H_0|z_j y_{j+1}\rangle = H_0|x_j z_{j+1}\rangle = 0, \\ H_0|y_j x_{j+1}\rangle &= J|z_j z_{j+1}\rangle, \quad H_0|z_j z_{j+1}\rangle = J|y_j x_{j+1}\rangle, \end{aligned} \quad (13)$$

while for states in $W_\ell = -1$ sector, one has

$$\begin{aligned} H_0|x_j x_{j+1}\rangle &= H_0|y_j y_{j+1}\rangle = 0, \\ H_0|z_j x_{j+1}\rangle &= -J|y_j x_{j+1}\rangle, \quad H_0|y_j z_{j+1}\rangle = -J|z_j x_{j+1}\rangle. \end{aligned} \quad (14)$$

We will use these relations to derive the Floquet Hamiltonian of the driven spin chain in Sec. III.

B. Dimensions of different sectors

In this section, we compute the HSD of the $W_\ell = 1$ and $W_\ell = \{\dots 1, 1, -1 \dots\}$ sectors of the spin model.

We first consider the sector where $W_\ell = +1$ for all ℓ . Guided by Eq. 8, we find that the number of states in this sector for a system of length L can be found by first defining a 8×8 transfer matrix $T_{j,mn}^{++++}$ at site j , where $m = (abc)$ and $n = (a'b'c')$ denote the row and column indices, and (abc) , $(a'b'c')$ can take the eight possible values xyx , xzy , xzz , yxy , yxz , zyx , zzy , zzz . The superscript $+++$ in T_j^{++++} signifies that this transfer matrix covers four sites $(j, j+1, j+2, j+3)$ with states satisfying $W_\ell = W_{\ell+1} = W_{\ell+2} = +1$.

The matrix element $T_{j,mn}^{++++}$ takes the value 1 if $m = (abc)$, $n = (bcd)$, where $(abcd)$ is an allowed state at the four consecutive sites $(j, j+1, j+2, j+3)$ satisfying $W_\ell = W_{\ell+1} = W_{\ell+2} = 1$, while $T_{j,mn}^{++++} = 0$ in all other cases. To be explicit, we have

$$T_j^{++++} = \begin{pmatrix} 0 & 0 & 0 & 1 & 1 & 0 & 0 & 0 \\ 0 & 0 & 0 & 0 & 0 & 1 & 0 & 0 \\ 0 & 0 & 0 & 0 & 0 & 0 & 1 & 1 \\ 1 & 0 & 0 & 0 & 0 & 0 & 0 & 0 \\ 0 & 1 & 1 & 0 & 0 & 0 & 0 & 0 \\ 0 & 0 & 0 & 1 & 1 & 0 & 0 & 0 \\ 0 & 0 & 0 & 0 & 0 & 1 & 0 & 0 \\ 0 & 0 & 0 & 0 & 0 & 0 & 1 & 1 \end{pmatrix}. \quad (15)$$

The eigenvalues of T_j^{++++} are given by τ , $-1/\tau$ and zero (appearing six times), where $\tau = (\sqrt{5}+1)/2$ is the golden ratio. Since the largest eigenvalue of T_j^{++++} is τ , the number of states in a system of length L grows as $\tau^L \simeq 1.618^L$ as $L \rightarrow \infty$. We note that the dependence of the HSD on L is identical to that for PXP model describing experimentally realizable Rydberg chains [18–21, 99] hosting Floquet QMBS [67, 70]. Such scars have also been identified in the present model in Ref. 97.

Next, we consider the sector with $W_\ell = \{\dots 1, 1, -1 \dots\}$. To find the number of states in this sector, we define three transfer matrices, denoted T_j^{++-} , T_j^{+-+} , and T_j^{-++} as described below. Then the number of states in this sector for a system with L sites will be given by $(\lambda_{max})^{L/3}$, where λ_{max} is the largest eigenvalue of the matrix $T_j^{++-} T_{j+1}^{+-+} T_{j+2}^{-++}$.

The transfer matrix $T_{j,mn}^{++-}$ covers four sites $(j, j+1, j+2, j+3)$, where $m = (abc)$ denotes states satisfying $W_\ell = W_{\ell+1} = +1$ and $n = (bcd)$ denotes states satisfying $W_{\ell+1} = +1$, $W_{\ell+2} = -1$. From Eqs. 8 and 9, we find that T_j^{++-} must be a 8×7 matrix, with m taking eight possible values xyx , xzy , xzz , yxy , yxz , zyx , zzy , zzz , and n taking seven possible values xyy , xyz , xzx , yxx , zyy , zyz , zzx . Using this, we find that

$$T_j^{++-} = \begin{pmatrix} 0 & 0 & 0 & 1 & 0 & 0 & 0 \\ 0 & 0 & 0 & 0 & 1 & 1 & 0 \\ 0 & 0 & 0 & 0 & 0 & 0 & 1 \\ 1 & 1 & 0 & 0 & 0 & 0 & 0 \\ 0 & 0 & 1 & 0 & 0 & 0 & 0 \\ 0 & 0 & 0 & 1 & 0 & 0 & 0 \\ 0 & 0 & 0 & 0 & 1 & 1 & 0 \\ 0 & 0 & 0 & 0 & 0 & 0 & 1 \end{pmatrix}. \quad (16)$$

Next, $T_{j,mn}^{+-+}$ is a transfer matrix covering four sites $(j, j+1, j+2, j+3)$, where $m = (abc)$ denotes states satisfying $W_\ell = +1$, $W_{\ell+1} = -1$ and $n = (bcd)$ denotes states satisfying $W_{\ell+1} = -1$, $W_{\ell+2} = +1$. We find that T_j^{+-+} must be a 7×7 matrix, with m taking seven possible values xyy , xyz , xzx , yxx , zyy , zyz , zzx , and n taking seven possible values xyx , xzx , yyx , yzx , yzz , zxy , zxx . From this observation, we find that

$$T_j^{+-+} = \begin{pmatrix} 0 & 0 & 1 & 0 & 0 & 0 & 0 \\ 0 & 0 & 0 & 1 & 1 & 0 & 0 \\ 0 & 0 & 0 & 0 & 0 & 1 & 1 \\ 1 & 1 & 0 & 0 & 0 & 0 & 0 \\ 0 & 0 & 1 & 0 & 0 & 0 & 0 \\ 0 & 0 & 0 & 1 & 1 & 0 & 0 \\ 0 & 0 & 0 & 0 & 0 & 1 & 1 \end{pmatrix}. \quad (17)$$

Finally, $T_{j,mn}^{-++}$ is a transfer matrix covering four sites $(j, j+1, j+2, j+3)$, where $m = (abc)$ denotes states satisfying $W_\ell = -1$, $W_{\ell+1} = +1$ and $n = (bcd)$ denotes states satisfying $W_{\ell+1} = +1$, $W_{\ell+2} = +1$. We find that T_j^{-++} must be a 7×8 matrix, with m taking seven possible values xyx , xzx , yyx , yzx , yzz , zxy , zxx , and n taking eight possible values xyx , xzy , xzz , yxy , yxz , zyx , zzy , zzz . This allows us to write

$$T_j^{-++} = \begin{pmatrix} 1 & 0 & 0 & 0 & 0 & 0 & 0 & 0 \\ 0 & 1 & 1 & 0 & 0 & 0 & 0 & 0 \\ 0 & 0 & 0 & 1 & 1 & 0 & 0 & 0 \\ 0 & 0 & 0 & 0 & 0 & 1 & 0 & 0 \\ 0 & 0 & 0 & 0 & 0 & 0 & 1 & 1 \\ 1 & 0 & 0 & 0 & 0 & 0 & 0 & 0 \\ 0 & 1 & 1 & 0 & 0 & 0 & 0 & 0 \end{pmatrix}. \quad (18)$$

Using Eqs. 16, 17 and 18, we find that the largest value of the magnitudes of the eigenvalues of $T_j^{+-}T_{j+1}^{++}T_{j+2}^{++}$ is about 3.7321. We therefore conclude that the number of states in this sector grows as $3.7321^{L/3} \simeq 1.5511^L$ as $L \rightarrow \infty$. This agrees with the results in Ref. 96 and 97.

Overall, we find that the HSD of each sectors is drastically reduced due to the presence of conserved W_ℓ . Since these sectors are dynamically disconnected, this allows us to study the dynamics of the spin chain in each sector using ED for $L \leq 24$, a system size which is otherwise impossible to address via ED for a spin-1 chain.

III. FLOQUET PERTURBATION THEORY

In this section we study the driven spin chain and obtain an analytic form of the first-order Floquet Hamiltonian for large drive amplitude. In what follows, we will drive H_1 using a square pulse protocol with a period $T = 2\pi/\omega_D$, where ω_D is the drive frequency, described in Eq. 2. We will restrict ourselves to the large drive amplitude regime for which $Q_0 \gg J$. In this case, the leading term in the evolution operator of the driven chain can be written as

$$U(t, 0) \equiv U_0(t) = e^{iQ_0 t \sum_j (S_j^x S_{j+1}^y)^2 / \hbar} \quad \text{for } t \leq T/2 \\ = e^{iQ_0 (T-t) \sum_j (S_j^x S_{j+1}^y)^2 / \hbar} \quad \text{for } T/2 < t \leq T. \quad (19)$$

At this order, we have $U_0(T, 0) = I$ which yields $H_F^{(0)} = 0$.

The first-order correction to the evolution operator $U(T, 0)$ is given by

$$U_1(T, 0) = -\frac{i}{\hbar} \int_0^T dt U_0^\dagger(t, 0) H_0 U_0(t, 0) = U_1^{(1)}(T, 0) + U_1^{(2)}(T, 0), \\ U_1^{(1)}(T, 0) = -\frac{i}{\hbar} \int_0^{T/2} dt e^{-iQ_0 t \sum_j (S_j^x S_{j+1}^y)^2 / \hbar} H_0 e^{iQ_0 t \sum_j (S_j^x S_{j+1}^y)^2 / \hbar}, \\ U_1^{(2)}(T, 0) = -\frac{i}{\hbar} \int_{T/2}^T dt e^{-iQ_0 (T-t) \sum_j (S_j^x S_{j+1}^y)^2 / \hbar} H_0 e^{iQ_0 (T-t) \sum_j (S_j^x S_{j+1}^y)^2 / \hbar}. \quad (20)$$

We first compute the first term in Eq. 20. To this end, we resolve U_0 using the eigenstates $|p\rangle$ of H_1 . These are the Fock states as can be seen from Eqs. 11 and 12. Using Eq. 10 with $\epsilon_p = pQ_0$, we can write, for $t \leq T/2$,

$$U_0(t, 0) = \sum_p e^{i\epsilon_p t / \hbar} |p\rangle \langle p|. \quad (21)$$

In terms of these eigenstates, we can write

$$U_1^{(1)}(T, 0) = -\frac{iT}{2\hbar} \sum_{p,q} \frac{\sin(\epsilon_p - \epsilon_q)T / (4\hbar)}{(\epsilon_p - \epsilon_q)T / (4\hbar)} \\ \times e^{i(\epsilon_p - \epsilon_q)T / (4\hbar)} \langle p | H_0 | q \rangle |p\rangle \langle q|. \quad (22)$$

A similar result is easily obtained for $U_1^{(2)}$ leading to $U_1(T, 0) = 2U_1^{(1)}(T, 0)$. To make further progress, we need to analyze the matrix elements $\langle p | H_0 | q \rangle$. The properties of these matrix elements depend on the sector being addressed. The analysis of the properties of these matrix

elements is carried out for the $W_\ell = 1$ sector in Sec. III A and the $W_\ell = \{\dots, 1, 1, -1, \dots\}$ sector in Sec. III B.

A. Analysis for the sector with all $W_\ell = 1$

In this subsection, we will first analyze the matrix elements and derive an explicit form of the first-order Floquet Hamiltonian in Sec. III A 1. This will be followed by an explicit counting of the HSD of the Floquet Hamiltonian at the special drive frequencies in Sec. III A 2.

1. First-order Floquet Hamiltonian for the sector with all $W_\ell = 1$

We begin by analyzing the matrix elements of $(H_0)_{pq} \equiv \langle p | H_0 | q \rangle$. We find that in the $W_\ell = 1$ sector, there are three classes of such terms. Using Eq. 13, we find that the only non-zero matrix elements correspond to

$$\begin{aligned}
T_1 &= \langle \cdots x_{j-1} y_j x_{j+1} y_{j+2} \cdots | S_j^x S_{j+1}^y | \cdots x_{j-1} z_j z_{j+1} y_{j+2} \cdots \rangle, \\
T_2 &= \langle \cdots x_{j-1} y_j x_{j+1} z_{j+2} \cdots | S_j^x S_{j+1}^y | \cdots x_{j-1} z_j z_{j+1} z_{j+2} \cdots \rangle, \\
T_3 &= \langle \cdots z_{j-1} y_j x_{j+1} y_{j+2} \cdots | S_j^x S_{j+1}^y | \cdots z_{j-1} z_j z_{j+1} y_{j+2} \cdots \rangle, \\
T_4 &= \langle \cdots z_{j-1} y_j x_{j+1} z_{j+2} \cdots | S_j^x S_{j+1}^y | \cdots z_{j-1} z_j z_{j+1} z_{j+2} \cdots \rangle,
\end{aligned} \tag{23}$$

and their Hermitian conjugates. From Eq. 11, one finds that T_1 corresponds to a process for which $\epsilon_p = \epsilon_q$ since $|\cdots x_{j-1} y_j x_{j+1} y_{j+2} \cdots\rangle$ and $|\cdots x_{j-1} z_j z_{j+1} y_{j+2} \cdots\rangle$ are eigenstates of H_1 with the same eigenvalue. Similarly for T_2 and T_3 , the states correspond to $\epsilon_p - \epsilon_q = Q_0$ and for T_4 , they correspond to $\epsilon_p - \epsilon_q = 2Q_0$. Moreover, inspecting the structure of the Fock states involved in these matrix elements one can define the operators

$$\begin{aligned}
H_a &= \sum_j P_{j-1}^x S_j^x S_{j+1}^y P_{j+2}^y, \\
H_b &= \sum_j (P_{j-1}^x P_{j+2}^z + P_{j-1}^z P_{j+2}^y) S_j^x S_{j+1}^y P_j^z P_{j+1}^z, \\
H_c &= \sum_j P_{j-1}^z S_j^x S_{j+1}^y P_j^z P_{j+1}^z P_{j+2}^z,
\end{aligned} \tag{24}$$

where $P_j^\alpha = (1 - (S_j^\alpha)^2)$ is a projection operator which projects the local spin on site j to $|\alpha\rangle$, with $|\alpha\rangle = |x\rangle, |y\rangle$ or $|z\rangle$. In terms of these operators, one can write $T_1 = \langle p | H_a | q \rangle$, $T_2 + T_3 = \langle p | H_b | q \rangle$ and $T_4 = \langle p | H_c | q \rangle$.

Substituting Eqs. 23 and 24 in Eq. 22, we find

$$\begin{aligned}
U_1(T, 0) &= -\frac{iJT}{\hbar} \left[H_a + \frac{\sin x}{x} (H_b e^{ix} + \text{H.c.}) \right. \\
&\quad \left. + \frac{\sin 2x}{2x} (H_c e^{2ix} + \text{H.c.}) \right],
\end{aligned} \tag{25}$$

where $x = Q_0 T / (4\hbar)$. Using the relation $H_F^{(1)} = i\hbar U_1(T, 0) / T$, we finally obtain

$$\begin{aligned}
H_F^{(1)} &= J \left[H_a + \frac{\sin x}{x} (H_b e^{ix} + \text{H.c.}) \right. \\
&\quad \left. + \frac{\sin 2x}{2x} (H_c e^{2ix} + \text{H.c.}) \right].
\end{aligned} \tag{26}$$

Eq. 26 indicates that there are two classes of special drive frequencies. The first of these occur at $\omega_n^* = Q_0 / (2n\hbar)$, where $n \in \mathbb{Z}$. At these frequencies, the first-order Floquet Hamiltonian is given by $H_F^{(1)} = JH_a$. From Eq. 24, we find that H_a involves projection operators which annihilates an exponentially large number of states in the Hilbert space of H . This is an indication that such a Floquet Hamiltonian may lead to a large number of frozen zero energy eigenstates and hence may support a Floquet realization of HSF [77].

The second class of such drive frequencies occurs at $\omega_n' = Q_0 / [(2n+1)\hbar]$, where $H_F^{(1)} = H_a + H_b / [(n+1/2)\pi]$. As we will see in the next section, this leads to a weak HSF. We note these two frequencies will show distinct behaviors for small n ; for larger n , the dynamics of the driven chain at these two frequencies will display close similarities due to the dominance of H_a in $H_F^{(1)}$.

2. HSD at special drive frequencies for all $W_\ell = 1$

To establish this intuition in a more concrete manner, we provide an explicit counting of the number of fragments corresponding to H_a . To this end, we resort to the transfer matrix formalism developed in Sec. II B. We note that H_a can only produce transitions between the states $|\cdots x_{j-1} y_j x_{j+1} y_{j+2}\rangle$ and $|\cdots x_{j-1} z_j z_{j+1} y_{j+2}\rangle$ at any four sites $(j-1, j, j+1, j+2)$, since this is the only pair of states for which $\Delta\epsilon = (\epsilon_p - \epsilon_q) = 0$. To count the number of different fragments, we therefore remove states of the form $|\cdots x_{j-1} z_j z_{j+1} y_{j+2}\rangle$ at any four sites since such states lie in the same fragment as the state $|\cdots x_{j-1} y_j x_{j+1} y_{j+2}\rangle$ because these two states are connected to each other by H_a . The number of fragments is therefore given by another transfer matrix $S_{j,mn}^{+++}$, where $S_{j,mn}^{+++}$ is just obtained from $T_{j,mn}^{+++}$ (Eq. 15) by changing the matrix element $T_{j,14}^{+++}$ from 1 to 0. We thus have

$$S_j^{+++} = \begin{pmatrix} 0 & 0 & 0 & 1 & 1 & 0 & 0 & 0 \\ 0 & 0 & 0 & 0 & 0 & 1 & 0 & 0 \\ 0 & 0 & 0 & 0 & 0 & 0 & 0 & 1 \\ 1 & 0 & 0 & 0 & 0 & 0 & 0 & 0 \\ 0 & 1 & 1 & 0 & 0 & 0 & 0 & 0 \\ 0 & 0 & 0 & 1 & 1 & 0 & 0 & 0 \\ 0 & 0 & 0 & 0 & 0 & 1 & 0 & 0 \\ 0 & 0 & 0 & 0 & 0 & 0 & 1 & 1 \end{pmatrix}. \tag{27}$$

We find that the largest value of the magnitudes of the eigenvalues of S_j^{+++} is about 1.5499. Hence the number of fragments grows as 1.5499^L as $L \rightarrow \infty$.

L	N_f	N_{fr}	\mathcal{D}_L
12	192 (192)	118 (129)	18 (18)
14	458 (462)	281 (291)	29 (29)
16	1107 (1108)	673 (655)	47 (47)
18	2667 (2663)	1495 (1472)	76 (76)
20	6403 (6398)	3281 (3311)	123 (123)
22	15370 (15370)	7393 (7449)	199 (199)
24	36920 (36922)	16782 (16753)	322 (322)

TABLE I. Comparison between exact numerics and analytical results (shown in brackets and rounded off to the nearest integer) for fragment number N_f , number of frozen fragments N_{fr} , and the HSD of the largest fragment \mathcal{D}_L for $H_F^{(1)} = H_a$ at $\hbar\omega_D = Q_0 / (2n)$. All results are for the sector with all $W_\ell = 1$. See text for details

Next, we can find the size of the largest fragment as follows. After some inspection, we find

that this is the fragment which contains the state $|\cdots y_{j-1}x_j y_{j+1}x_{j+2}y_{j+3}x_{j+4}y_{j+5}x_{j+6}\cdots\rangle \equiv |\cdots xyxyxyx\cdots\rangle$. The state of any four sites can change from $|xyxy\rangle$ to $|xzzz\rangle$. However, since H_a does not allow the transitions $|zyxy\rangle \leftrightarrow |zzzz\rangle$ and $|xyxz\rangle \leftrightarrow |xzzz\rangle$, a transition from either $|xzzzyxy\rangle$ or $|xyxzzzy\rangle$ to $|xzzzzzy\rangle$ is not allowed. Hence the state $|xyxyxy\rangle$ cannot change, in two steps, to $|xzzzzzy\rangle$. Thus the fragment containing $|\cdots xyxyxyx\cdots\rangle$ only contains states in which any two sites yx can be replaced by zz but two zz 's are not allowed to sit next to each other. This resembles the PXP model in which there is a spin-1/2 at each site and there is a constraint that two spin-1/2's cannot sit next to each other.

To make this mapping from the sector with all $W_\ell = 1$ and with the constraint $\Delta\epsilon = 0$ to the PXP model more precise, we replace the pair yx by a spin-down and the pair zz by a spin-up. If our model has L sites, the PXP model has $L/2$ sites. The number of states in the PXP model with $L/2$ sites is known to be $\tau^{L/2}$. Hence the size of the largest fragment grows as 1.2720^L . We thus see that the ratio of the size of the largest fragment to the size of the full sector is given by $\tau^{L/2}/\tau^L$ which goes to zero exponentially as 0.7862^L as $L \rightarrow \infty$. Hence we have a strong prethermal HSF at the special driving frequencies in the $W_\ell = 1$ sector.

L	N_f	HSD of fragments
6	6	1, 1, 1, 1, 7, 7
8	4	1, 15, 15, 16
10	4	1, 31, 31, 60
12	7	1, 1, 1, 1, 63, 63, 192
14	5	1, 28, 127, 127, 560
16	5	1, 160, 255, 255, 1536
18	8	1, 1, 1, 1, 511, 511, 720, 4032
20	6	1, 40, 1023, 1023, 2800, 10240
22	6	1, 308, 2047, 2047, 9856, 25344
24	9	1, 1, 1, 1, 1792, 4095, 4095, 32256, 61440
26	7	1, 52, 8191, 8191, 8736, 99840, 146432
28	7	1, 504, 16383, 16383, 37632, 295680, 344064

TABLE II. Table showing the number of fragments N_f and their HSD's for different L . We have taken the spin chain to have periodic boundary conditions; all results are for the $W_\ell = 1$ sector, and $\omega_D = \omega'_1 = Q_0/\hbar$ where $H_F^{(1)} = H_a + 2H_b/\pi$. See text for details.

Finally, we can find the number of frozen fragments; these are fragments which have only one state each. Hence these states are zero energy eigenstates of the first-order Floquet Hamiltonian. The number of frozen fragments can be found by simply removing the two states $|xyxy\rangle$ and $|xzzz\rangle$ at any four sites since these are the only states between which transitions are allowed by the Hamiltonian. We can therefore define another transfer matrix which is obtained from $T_{j,mn}^{++++}$ by setting the ma-

trix elements $(mn) = (14)$ and (37) equal to zero. The largest value of the magnitudes of the eigenvalues of this matrix is found to be about 1.4997. Hence the number of frozen fragments grows as 1.4997^L as $L \rightarrow \infty$. These analytical results show excellent match with exact numerics as can be seen in Table I.

Eq. 26 also indicates that for the special frequencies $\omega'_n = Q_0/((2n+1)\hbar)$, the first-order Floquet Hamiltonian contains H_a, H_b and its Hermitian conjugate but does not contain H_c . We will now show that this also leads to a HSF which is different from the case discussed above where the first-order Floquet Hamiltonian only contains H_a . This can be quantified as follows.

To find the number of fragments and the size of the largest fragment in this case, we resort to a numerical counting for the first few values of L (chosen to be even) with periodic boundary conditions. These are shown in Table II. We see that as the system size L increases, the number of fragments grows only linearly (increasing by 1 whenever L increases by 6), while the size of the largest fragment grows exponentially. Since we know that the total number of states grows asymptotically as 1.618^L , the size of the largest fragment must also grow exponentially in the same way if the number of fragments only grows linearly with L .

Finally, we can find the number of frozen fragments which have only one state each. The number of such fragments can be found by removing the six states having combinations $|xyxy\rangle, |xzzz\rangle, |xyxz\rangle, |xzzz\rangle, |zyxy\rangle$ and $|zzzz\rangle$ at any four sites since these are the only states between which transitions are allowed by the Hamiltonian. We therefore define another transfer matrix which is obtained from $T_{j,mn}^{++++}$ by setting the matrix elements $(mn) = (14), (37), (15), (38), (64)$ and (87) equal to zero. We find that this matrix has four eigenvalues λ_i equal to 1, and the other four eigenvalues are equal to zero. Hence, for a system with L sites and periodic boundary conditions, the number of frozen fragments does not grow exponentially with L . We find that the number is 4 if L is a multiple of 3 and is 1 if L is not a multiple of 3 (see Table II). This can be understood as follows. For all values of L , we find that one of the fragments consists of the state $|\cdots zzzzzz\cdots\rangle$. When L is a multiple of 3, we find three other frozen fragments which are given by three period-three states; one of these is $|\cdots zyxyxy\cdots\rangle$ while the other two states are related to this state by translations.

Based on an inspection of systems with size up to $L = 12$ and periodic boundary conditions, we have the following understanding of the growth of the number of fragments with L given in Table II. For this purpose, we use the idea of a *root state* [83, 84]. This is defined as one particular state defined in each fragment such that all states in that fragment can be connected to that state by repeated actions of the first-order Floquet Hamiltonian. The number of root states is equal to the number of fragments. There are many ways of choosing the root states; hence we have to specify them in a particular way as

discussed below.

We find that the root states have one of the following forms. First, we have the frozen fragments which have only one state each; as discussed above, their number is four if L is a multiple of 3 and unity if L is not a multiple of 3. Next, there are two fragments with root states which have the states $|\cdots yxyx \cdots yx \cdots\rangle$ and $|\cdots xyxy \cdots xy \cdots\rangle$ from sites 1 to L ; these fragments have $2^{L/2} - 1$ states each. Finally, the other fragments have root states which have $|\cdots yxzyxzyxz \cdots zzzz \cdots\rangle$ from sites 1 to L . Namely, these root states have some repeated strings of yxz 's followed at the end by one or more z 's. The number of yxz strings can range from 2, 4, 6, \cdots , up to the largest even integer which is less than $L/3$. The total number of fragments obtained in this way agrees with the numbers n_f given in Table II.

We note that the higher order terms in the Floquet Hamiltonian do not support the two kinds of HSF discussed above (i.e., when only H_a is present, and when H_a, H_b and its Hermitian conjugate are present). However, as we will see in Sec. IV, the dynamics of the driven chain will bear distinct signatures of the fragmentation

over a long prethermal timescale in the regime of large drive amplitude.

B. Analysis for $W_\ell = \{\cdots 1, 1, -1 \cdots\}$ sector

In this subsection, we analyze the matrix elements $\langle p|H_0|q\rangle$ for the $W_\ell = \{\cdots 1, 1, -1 \cdots\}$ sector. We derive the first-order Floquet Hamiltonian in Sec. III B 1. This is followed by Sec. III B 2 where we find the HSD of the Floquet Hamiltonian at the special drive frequencies.

1. First-order Floquet Hamiltonian for the $W_\ell = \{\cdots 1, 1, -1 \cdots\}$

To analyze the matrix elements in the $W_\ell = \{\cdots 1, 1, -1 \cdots\}$ sector, we note that there are three possible combinations of the Z_2 -valued conserved quantities. Each of these connect distinct states via action of H_0 . For example, for the arrangement (1, 1 - 1) in three consecutive links with the middle sites labeled by j and $j + 1$, we find the non-zero matrix elements to be

$$\begin{aligned} T'_1 &= \langle \cdots x_{j-1} y_j x_{j+1} x_{j+2} \cdots | S_j^x S_{j+1}^y | \cdots x_{j-1} z_j z_{j+1} x_{j+2} \cdots \rangle, \\ T'_2 &= \langle \cdots z_{j-1} y_j x_{j+1} x_{j+2} \cdots | S_j^x S_{j+1}^y | \cdots z_{j-1} z_j z_{j+1} x_{j+2} \cdots \rangle. \end{aligned} \quad (28)$$

The first of these processes corresponding to T'_1 has $\Delta\epsilon = \epsilon_p - \epsilon_q = Q_0$ while that corresponding to T'_2 has $\Delta\epsilon = 2Q_0$. Next, for the arrangement $W_\ell = (1, -1, 1)$, we find the matrix elements to be

$$\begin{aligned} T'_3 &= \langle \cdots x_{j-1} y_j z_{j+1} y_{j+2} \cdots | S_j^x S_{j+1}^y | \cdots x_{j-1} z_j x_{j+1} y_{j+2} \cdots \rangle, \\ T'_4 &= \langle \cdots z_{j-1} y_j z_{j+1} y_{j+2} \cdots | S_j^x S_{j+1}^y | \cdots z_{j-1} z_j x_{j+1} y_{j+2} \cdots \rangle, \\ T'_5 &= \langle \cdots z_{j-1} y_j z_{j+1} z_{j+2} \cdots | S_j^x S_{j+1}^y | \cdots z_{j-1} z_j x_{j+1} z_{j+2} \cdots \rangle, \\ T'_6 &= \langle \cdots x_{j-1} y_j z_{j+1} z_{j+2} \cdots | S_j^x S_{j+1}^y | \cdots x_{j-1} z_j x_{j+1} z_{j+2} \cdots \rangle, \end{aligned} \quad (29)$$

which correspond to $\Delta\epsilon = 0$ for T'_3 and T'_5 and $\Delta\epsilon = Q_0$ for T'_4 and T'_6 . Finally, for the arrangement $W_\ell = (-1, 1, 1)$, one has

$$\begin{aligned} T'_7 &= \langle \cdots y_{j-1} y_j x_{j+1} y_{j+2} \cdots | S_j^x S_{j+1}^y | \cdots y_{j-1} z_j z_{j+1} y_{j+2} \cdots \rangle, \\ T'_8 &= \langle \cdots y_{j-1} y_j x_{j+1} z_{j+2} \cdots | S_j^x S_{j+1}^y | \cdots y_{j-1} z_j z_{j+1} z_{j+2} \cdots \rangle, \end{aligned} \quad (30)$$

which correspond to $\Delta\epsilon = Q_0$ and $\Delta\epsilon = 2Q_0$ respectively.

From these matrix elements it is easy to see, following the analysis of Sec. III A, that one may write down the

operators

$$\begin{aligned} H'_a &= \sum_j (P_{j-1}^x P_{j+2}^y + P_{j-1}^z P_{j+2}^z) S_j^x S_{j+1}^y, \\ H'_b &= \sum_j \left[(P_{j-1}^x P_{j+2}^x + P_{j-1}^y P_{j+2}^y) S_j^x S_{j+1}^y P_j^z P_{j+1}^z \right. \\ &\quad \left. + (P_{j-1}^z P_{j+2}^y + P_{j-1}^x P_{j+2}^z) S_j^x S_{j+1}^y P_j^z P_{j+1}^x \right] \quad (31) \\ H'_c &= \sum_j (P_{j-1}^z P_{j+2}^x + P_{j-1}^y P_{j+2}^z) S_j^x S_{j+1}^y P_j^z P_{j+1}^z. \end{aligned}$$

In terms of these operators one can write $T'_3 + T'_5 = \langle p|H'_a|q\rangle$, $T'_1 + T'_4 + T'_6 + T'_7 = \langle p|H'_b|q\rangle$ and $T'_2 + T'_8 = \langle p|H'_c|q\rangle$. Then an analysis exactly to the one carried out in Sec. III A yields

$$H'_F{}^{(1)} = J \left[H'_a + \frac{\sin x}{x} (H'_b e^{ix} + \text{H.c.}) + \frac{\sin 2x}{2x} (H'_c e^{2ix} + \text{H.c.}) \right]. \quad (32)$$

Once again, at the special frequency $\omega_n^* = Q_0/(2n\hbar)$, the first-order Floquet Hamiltonian is given by JH'_a . We therefore once again expect a realization of prethermal strong HSF at these frequencies. We will verify this expectation both analytically and numerically in the next subsection.

2. *HSD at special drive frequencies for the sector*
 $W_\ell = \{\dots 1, 1, -1 \dots\}$

To put these ideas on a solid mathematical footing, we count the number of different fragments similar to that done for the $W_\ell = 1$ sector. Here we note that the transitions corresponding to $\Delta\epsilon = 0$ connect the states $|\dots x_{j-1} y_j z_{j+1} y_{j+2} \dots\rangle \equiv |xyzzy\rangle \leftrightarrow |\dots x_{j-1} z_j x_{j+1} y_{j+2} \dots\rangle \equiv |xzxxy\rangle$, and the states $|zyzz\rangle \leftrightarrow |zzxz\rangle$ at any four sites $(j-1, j, j+1, j+2)$ for which $W_\ell = \{1, -1, 1\}$. Hence we remove states of the form $|xzxxy\rangle$ and $|zzxz\rangle$ at such sites, since these states lie in the same fragment as the states $|xyzzy\rangle$ and $|zyzz\rangle$ respectively. We therefore replace the transfer matrix $T_{j,mn}^{+-+}$ by another transfer matrix $S_{j,mn}^{+-+}$, where $S_{j,mn}^{+-+}$ is obtained from $T_{j,mn}^{+-+}$ by changing the matrix elements $T_{j,36}^{+-+}$ and $T_{j,77}^{+-+}$ from 1 to 0. We thus have

$$S_j^{+-+} = \begin{pmatrix} 0 & 0 & 1 & 0 & 0 & 0 & 0 \\ 0 & 0 & 0 & 1 & 1 & 0 & 0 \\ 0 & 0 & 0 & 0 & 0 & 0 & 1 \\ 1 & 1 & 0 & 0 & 0 & 0 & 0 \\ 0 & 0 & 1 & 0 & 0 & 0 & 0 \\ 0 & 0 & 0 & 1 & 1 & 0 & 0 \\ 0 & 0 & 0 & 0 & 0 & 1 & 0 \end{pmatrix}. \quad (33)$$

We then find that the largest value of the magnitudes of the eigenvalues of $T_j^{+-+} S_{j+1}^{+-+} T_{j+2}^{+-+}$ is given by 3.1149. Hence the number of fragments grows as $3.1149^{L/3} \simeq 1.4604^L$ as $L \rightarrow \infty$. We have checked that these results do not change if we remove the states $|xyzzy\rangle$ instead of $|xzxxy\rangle$, and $|zyzz\rangle$ instead of $|zzxz\rangle$.

Next, we compute the number of frozen fragments; these are fragments with only one Fock state. To do this, we remove the states $|xyzzy\rangle$, $|xzxxy\rangle$, $|zyzz\rangle$ and $|zzxz\rangle$ at any four sites $(j-1, j, j+1, j+2)$ for which $W_\ell = 1, -1, 1$ since these states are connected to each other by the Floquet Hamiltonian. We therefore replace the transfer matrix $T_{j,mn}^{+-+}$ by another transfer matrix

$R_{j,mn}^{+-+}$, where $R_{j,mn}^{+-+}$ is obtained from $T_{j,mn}^{+-+}$ by changing the matrix elements $T_{j,24}^{+-+}$, $T_{j,36}^{+-+}$, $T_{j,65}^{+-+}$ and $T_{j,77}^{+-+}$ from 1 to 0. We thus have

$$R_j^{+-+} = \begin{pmatrix} 0 & 0 & 1 & 0 & 0 & 0 & 0 \\ 0 & 0 & 0 & 0 & 1 & 0 & 0 \\ 0 & 0 & 0 & 0 & 0 & 0 & 1 \\ 1 & 1 & 0 & 0 & 0 & 0 & 0 \\ 0 & 0 & 1 & 0 & 0 & 0 & 0 \\ 0 & 0 & 0 & 1 & 0 & 0 & 0 \\ 0 & 0 & 0 & 0 & 0 & 1 & 0 \end{pmatrix}. \quad (34)$$

We find that the largest value of the magnitudes of the eigenvalues of $T_j^{+-+} R_{j+1}^{+-+} T_{j+2}^{+-+}$ is given by 2.5616. Hence the number of fragments grows as $2.5616^{L/3} \simeq 1.3683^L$ as $L \rightarrow \infty$.

Finally, we find the largest fragment as follows. We first note that the state at the site j which lies between the bonds with $W_\ell = W_{\ell+1} = +1$ does not change at all under transitions for which $\epsilon = 0$. Hence we only have to consider the sites which lie at the ends of the bonds with $W_{\ell+2} = -1$. After some inspection, we find that the largest fragment is the one which contains the states $|zyzz\rangle$ and $|zzxz\rangle$ at sites $(j-1, j, j+1, j+2)$ which have $W_\ell = 1$, $W_{\ell+1} = -1$, $W_{\ell+2} = 1$. Since there are two possible states for every sequence of three such bonds, the size of this fragment is $2^{L/3} = 1.2599^L$. The ratio of the size of the largest fragment to the size of the full sector is given by $1.2599^L / 1.5511^L = 0.8123^L$ which goes to zero exponentially as $L \rightarrow \infty$. This proves the presence of prethermal HSF at the special frequencies. The analytical results obtained here matches those obtained from exact numerics quite well as can be seen from Table III.

L	N_f	N_{fr}	\mathcal{D}_L
6	11 (10)	10 (7)	4 (4)
12	95 (94)	50 (43)	16 (16)
18	914 (913)	298 (283)	64 (64)
24	8863 (8862)	1890 (1854)	256 (256)

TABLE III. Comparison between exact numerics and analytical results (shown in brackets and rounded off to the nearest integer) for the number of fragments N_f , number of frozen fragments N_{fr} , and the HSD of the largest fragment for different L , for the sector with $W_\ell = \{\dots 1, 1, -1 \dots\}$ and $\hbar\omega_D = Q_0/(2n)$. See text for details.

Since the largest fragment only contains Fock states with the sequences $|zyzz\rangle$ and $|zzxz\rangle$, it possesses an integrable structure. To see this, we note that the dynamics of such states can be described by a Hamiltonian of the form

$$H_{\text{eff}} = J \sum_k \tau_k^x, \quad (35)$$

where k takes $L/3$ possible values, and $\tau_k^z = +1$ and -1 denote the states $|zyzz\rangle$ and $|zzxz\rangle$ respectively. This

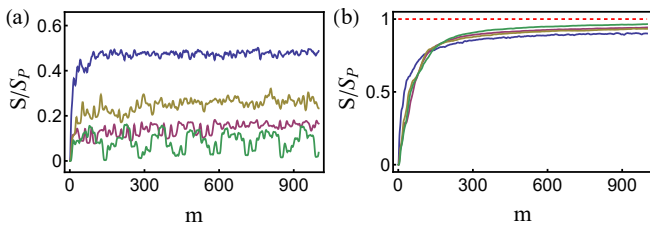


FIG. 2. (a) Plot of the half-chain entanglement $S_{L/2}(mT)/S_p \equiv S/S_p$ as a function of m at the special frequency $\omega_D = \omega_1^* = Q_0/(2\hbar)$ and for several different representative initial Fock states. The plot indicates that the saturation value of $S/S_p < 1$ at large m ; moreover, it depends on the chosen initial state. (b) In contrast, for $\omega_D = 1.2\omega_1^*$, an analogous plot for the same initial states leads to $S/S_p \rightarrow 1$. For both plots, $L = 24$, the initial states are chosen from the $W_\ell = 1$ sector, $Q_0/J = 100$, and all energies are in units of J .

constitutes a two-level (or, equivalently, decoupled spin-1/2) system for a given k . The dynamics in this sector is therefore particularly simple and mimics that of an integrable model.

For $\hbar\omega_D = Q_0/(2n+1)$, where $n \in \mathbb{Z}$, $H_F = H'_a + H'_b\pi/(n+1/2)$; we numerically find that in contrast to the $W_\ell = 1$ sector, the Hilbert space of H_F has a single fragment. Thus these frequencies do not lead to either strong or weak fragmentation (i.e., exponential or power-law growth of the number of fragments with L) for the $W_\ell = \{\dots, 1, 1, -1, \dots\}$ sector.

In the next section, we shall study the dynamics in both these sectors numerically using ED with the aim of finding signatures of strong HSF at the special drive frequencies.

IV. NUMERICAL RESULTS

In this section, we provide numerical support for our analytical results derived in Sec. III. We study the properties of the half-chain entanglement entropy of the driven chain in Sec. IV A. This is followed in Sec. IV B by a study of the fidelity of the driven state, starting from simple initial Fock states. Finally, we study the dynamics of a correlation function of the driven model in Sec. IV C.

A. Entanglement entropy

In this subsection we study the half-chain entanglement entropy $S_{L/2} \equiv S$ of the driven chain starting from several initial Fock states. To compute S , we follow the procedure outlined in Refs. 66 and 69. We start from an initial Fock state and evolve it up to m drive cycles to obtain the many-body state $|\psi(mT)\rangle = U(mT, 0)|\psi(0)\rangle$. Here $U(mT, 0)$ is the evolution operator of the system and $|\psi(0)\rangle$ is the initial state. To compute $U(mT, 0)$ for a square pulse protocol, we first numerically diagonalize

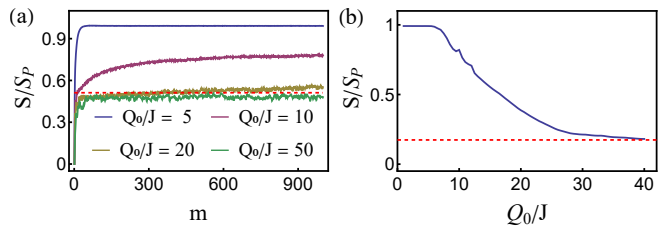


FIG. 3. (a) Plot of $S_{L/2}(mT)/S_p \equiv S/S_p$ as a function of n at the special frequency $\omega_D = \omega_1^* = Q_0/(2\hbar)$ and for several representative values of Q_0/J . The initial state is chosen to be a Fock state lying in the largest fragment of H_a ; the corresponding Page value of the fragmented sector, S_p^f , is indicated by the red-dashed line. (b) Plot of S_{av}/S_p as a function of Q_0/J showing a gradual crossover from ergodic to fragmented dynamics. For both plots, $L = 24$, the initial states are chosen from the $W_\ell = 1$ sector, $\omega_D = \omega_1^*$, and all energies are scaled in units of J .

the Hamiltonian $H_\pm = H[\pm Q_0]$ and find the corresponding eigenvalues ϵ_μ^\pm and eigenstates $|\mu_\pm\rangle$ via

$$H_\pm|\mu_\pm\rangle = \epsilon_\mu^\pm|\mu_\pm\rangle. \quad (36)$$

Using these eigenstates and eigenvalues, we can express the evolution operator as

$$U(mT, 0) = \sum_{\mu\nu} c_{\mu\nu}^\pm e^{-i(\epsilon_\mu^+ + \epsilon_\nu^-)mT/(2\hbar)} |\mu_+\rangle\langle\nu_-|, \quad (37)$$

where $c_{\mu\nu}^\pm = \langle\mu_+|\nu_-\rangle$. The density matrix corresponding to the state $|\psi(mT)\rangle$ can then be obtained as $\rho(mT) = |\psi(mT)\rangle\langle\psi(mT)|$. The reduced density matrix, computed from $\rho(mT)$ by numerically tracing out states which have weight on the subsystem B of length $L/2$ of the chain, is given by [66, 69]

$$\rho_{\text{red}}(mT) = \text{Tr}_B[\rho(mT)]. \quad (38)$$

The entanglement is obtained from the eigenvalues $\lambda_i(mT)$ of the reduced density matrix. These eigenvalues are obtained by numerical diagonalization of $\rho_{\text{red}}(mT)$ and the von Neumann entanglement entropy S is then obtained using

$$S(mT) = -\sum_i \lambda_i(mT) \ln \lambda_i(mT). \quad (39)$$

It is well-known that for an ergodic system, $S(mT)$ reaches its Page value, S_p , for $m \gg 1$ [36, 77, 100].

We first consider the dynamics of $S(mT)$ for the $W_\ell = 1$ sector. The plot of $S(mT)$ as a function of m is shown in Figs. 2(a) and (b). Fig. 2(a) shows that at the special drive frequencies $\omega_D = \omega_1^*$, $S(mT)/S_p < 1$ for all initial states; moreover the value to which $S(mT)/S_p$ saturates depends strongly on the chosen initial state. This indicates a retainment of the memory of the initial state and thus constitutes a clear violation of Floquet ETH which predicts $S/S_p \rightarrow 1$ for $m \rightarrow \infty$. Indeed the latter behavior is clearly seen when one moves away from the special

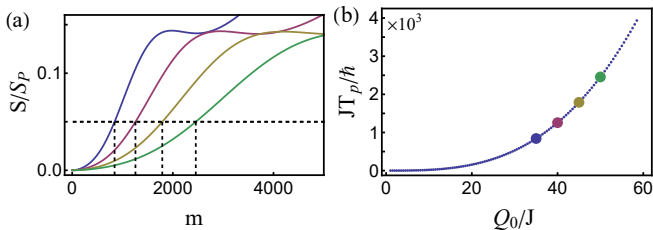


FIG. 4. (a) Plot of $S_{L/2}(mT)/S_p \equiv S/S_p$ as a function of m at the special frequency $\omega_D = \omega_1^* = Q_0/(2\hbar)$ and $Q_0/J = 35$ (blue), 40 (magenta), 45 (yellow), and 50 (green) for an initial frozen state $|\psi(0)\rangle = |\dots zzz \dots\rangle$ lying in the $W_\ell = 1$ sector. The dynamics of S/S_p is a consequence of higher order terms in the Floquet Hamiltonian. The prethermal timescale $T_p = m_p T$ is estimated from the number of drive cycles $m = m_p$ for which $S(mT)/S_p \simeq 0.05$. (b) Plot of JT_p/\hbar as a function of Q_0 keeping ω_D fixed at ω_1^* ; the data corresponding to panel (a) is shown by circles with same color code as in (a). For both plots, $L = 24$ and all energies are scaled in units of J . See text for details.

frequencies; for any initial state, $S(mT)/S_p$ approaches unity for large m as expected from Floquet ETH.

The deviation of $S(mT)/S_p$ from unity at large m and its dependence on the initial state is consistent with fragmentation of the Hilbert space at large drive amplitude where H_a dominates the dynamics. In the presence of such a fragmentation, the entanglement of a driven state saturates to the Page value of the sector to which it belongs, and different choices of the initial state lead to different values of the entanglement at large prethermal times [77].

Next, we study the behavior of $S(mT)$ as a function of m at the special frequency $\omega_D = \omega_1^*$ for several representative values of Q_0 . For this we have chosen the initial state to be $|\psi_1\rangle = |\dots xyxy \dots\rangle$ which belongs to the largest sector of H_a . The plot showing the behavior $S(mT)/S_p$ for different Q_0 is shown in Fig. 3(a). We find that at low Q_0 , the driven chain exhibits ergodicity and $S/S_p \rightarrow 1$ at large m . In contrast, for large Q_0/J , $S(mT)$ saturates to the Page value of the largest sector of H_a given by S_p^f shown by the red dotted line. In Fig. 3(b), we plot the average entanglement S_{av}/S_p as a function of Q_0 at $\omega_D = \omega_1^*$, where S_{av} is given by

$$S_{av} = \frac{1}{51} \sum_{n=325}^{375} S(mT). \quad (40)$$

We find that S_{av} interpolates between S_p at lower Q_0/J to S_p^f at higher Q_0/J , indicating a gradual crossover to a prethermal state exhibiting Floquet HSF.

To estimate this prethermal timescale over which the fragmentation occurs, we compute $S(mT)$ starting from a frozen product state of H_a given by $|\psi_2\rangle = |\dots zzzz \dots\rangle$. We note that if the dynamics is entirely controlled by $H_F^{(1)}$, $S(mT) = 0$ at the special frequency. Thus the deviation of $S(mT)$ from its zero value provides an estimate of the prethermal timescale beyond which correc-

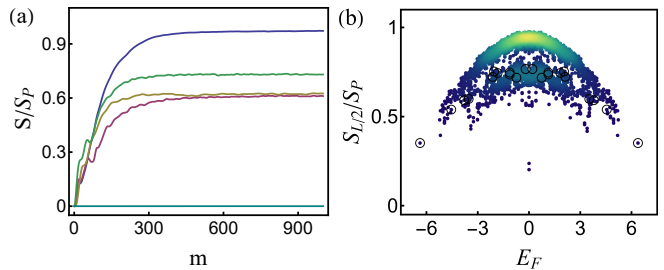


FIG. 5. (a) Plot of $S_{L/2}(mT)/S_p \equiv S/S_p$ as a function of m at $\hbar\omega_D = Q_0$, $L = 24$ and $Q_0/J = 40$ for several initial Fock states. S/S_p saturates to three distinct values showing signatures of weak fragmentation. (b) Plot of the half-chain entanglement $S_{L/2}/S_p$ for Floquet eigenstates as a function of their quasienergy E_F for $\hbar\omega_D = Q_0 = 40J$ for $L = 18$, showing two distinct clusters separated by a gap in S . For both plots, the initial states are chosen from the $W_\ell = 1$ sector, and all energies are scaled in units of J . See text for details.

tions to $H_F^{(1)}$ becomes important. A plot of $S(mT)/S_p$ for $\omega_D = \omega_1^*$ for several representative values of Q_0/J is shown in Fig. 4(a). This allows us to define the number of cycles $m = m_p$ for which $S(mT)/S_p \simeq 0.05$. We find that m_p increases with Q_0/J and provides an estimate of the prethermal timescale $T_p = m_p T$. A plot of the variation of T_p as a function of Q_0/J is shown in Fig. 4(b). We find that T_p grows exponentially with Q_0 which indicates that the prethermal timescale is exponentially large at large drive amplitudes. This conforms with the standard expectation for the dependence of the width of the prethermal regime on the drive amplitude [77, 89, 90].

Next, we compute the entanglement $S(mT)/S_p$ for the frequency $\hbar\omega_D = Q_0$ for which $H_F^{(1)} = H_a + 2H_B/\pi$. Here the driven system saturates to different long-time values of $S(mT)/S_p$. As shown in Fig. 5(a), for the majority of initial Fock states, $S(mT)/S_p \simeq 0.9$ for large m ; however, for other initial Fock states, $S(mT)/S_p \rightarrow 0.55, 0.7$ in the large m limit. This indicates the possibility of having a few dynamically disconnected fragments, one of which has a much larger HSD than the others. We note that the number of values to which $S(mT)$ saturates is much smaller than at $\omega_D = \omega_1^*$ shown in Fig. 2(a). This behavior is further supported by Fig. 5(b), where we plot S/S_p of the Floquet eigenstates as a function of their quasienergy E_F/J . The plot shows two distinct clusters of eigenstates with different entanglement entropies which is consistent with the behavior shown in Fig. 5(a). We stress that we do not find an exponentially large number of dynamically disconnected sectors at this drive frequency unlike at $\omega_D = \omega_n^*$.

Finally, we compute the entanglement entropy starting from initial states lying in the $W_\ell = \{\dots 1, 1, -1 \dots\}$ sector. To this end, we begin by choosing an initial Fock state $|\psi'_1\rangle = |\dots zyzyzy \dots\rangle$ or $|\psi'_2\rangle = |\dots yxyxyx \dots\rangle$ and compute $|\psi'(mT)\rangle = U(mT, 0)|\psi(0)\rangle$. The entanglement entropy $S(mT)$ is computed from the reduced den-

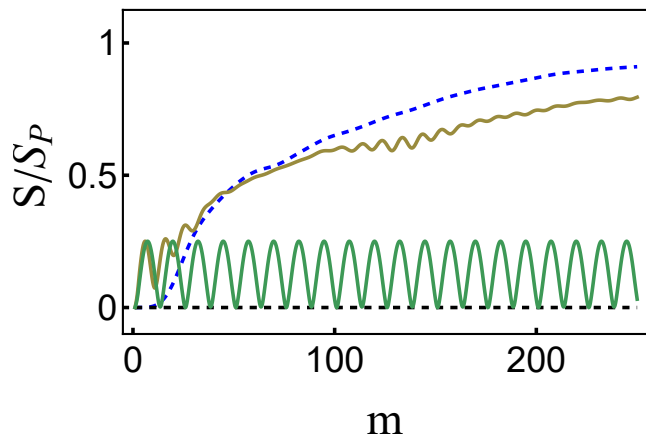


FIG. 6. Plot of $S_{L/2}(mT)/S_p \equiv S/S_p$ as a function of m at $\hbar\omega_D = Q_0$ (yellow solid line) $\hbar\omega_D = Q_0/2$ (green solid line) starting from the state $|\psi'_1\rangle$ which belongs to the largest fragment of H'_a . Similar plots starting from an initial frozen state $|\psi'_2\rangle$ is shown for $\hbar\omega_D = Q_0$ (blue dashed line) and $Q_0/2$ (black dashed line). For all the plots, $L = 24$, the initial states belong to the $W_\ell = \{\dots 1, 1, -1 \dots\}$ sector, $Q_0/J = 40$, and all energies are scaled in units of J . See text for details.

sity matrix corresponding to $|\psi'(mT)\rangle$ following the same procedure as described earlier for states in the $W_\ell = 1$ sector.

The behavior of $S(mT)/S'_p$, where $S'_p = 0.45$ is the Page value of the sector, is shown in Fig. 6. For the initial state $|\psi'_1\rangle$ we find that S/S_p increase towards the sector Page value if $\hbar\omega_D = Q_0$; a similar behavior (not shown in the figure) is found for the initial state $|\psi'_2\rangle$. We have numerically checked that such a growth of $S(mT)$ towards $S_p \simeq 0.45$ occurs for all $\hbar\omega_D \neq Q_0/(2n)$ (where $n \in \mathbb{Z}$) for any randomly chosen initial Fock state. This supports the absence of fragmentation at $\omega_D = \omega'_n$ in this sector.

In contrast, for $\hbar\omega_D = Q_0/2$, these two states show qualitatively different behaviors of $S(mT)$. For an initial state $|\psi'_1\rangle$, $S(mT)$ oscillates between its initial value of zero and the value of $\ln 2$. This can be understood by noting that the initial state $|\psi'_1\rangle$ belongs to the largest fragment of H'_a (Eq. 31). As shown in Sec. III B 2, the states in the largest sector can be described as those of $L/3$ decoupled spins described by Pauli matrices τ_k living on the links of the chain. Constructing the half-chain essentially amounts to severing one such link which may lead to $S = 0$ if the spin is in a S_z eigenstate and $\ln 2$ if it is in a singlet state or a triplet state with $m_z = 0$. These are therefore the two extremal possible value of S , and one finds an oscillation of $S(mT)$ between them. Such an oscillation is therefore a signature of the integrable nature of the largest fragment of H'_a . In contrast, the state $|\psi'_2\rangle$ is a frozen state, with $H'_a|\psi'_2\rangle = 0$. Thus $S(mT)$ remains close to its initial zero value for a large prethermal time scale, as shown by the green dashed line of Fig. 6. Such a dependence of $S(mT)$ on the initial state is an indication of a prethermal emergent HSF at special drive frequencies

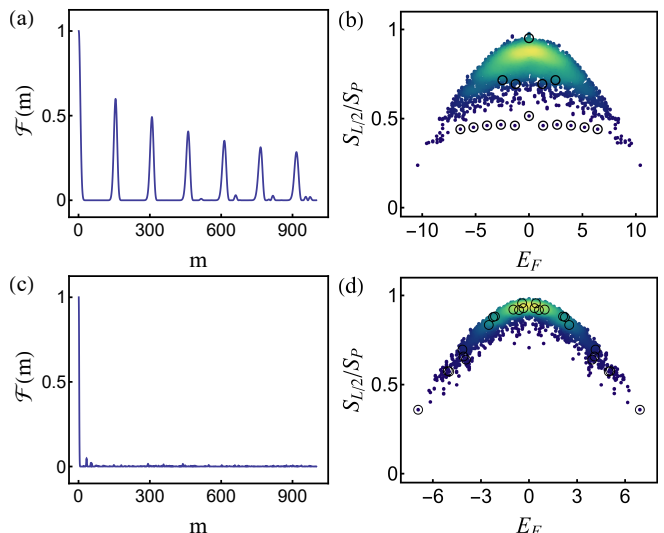


FIG. 7. (a) Plot of $\mathcal{F}(mT)$ as a function of the number of drive cycles m for $\hbar\omega_D/Q_0 = 5$. $\mathcal{F}(mT)$ shows an oscillatory behavior; the amplitudes of these oscillations decrease with m . (b) Plot of $S_{L/2}/S_p$ for all Floquet eigenstates as a function of their quasienergy E_F/J for $\hbar\omega_D/Q_0 = 5$. The plot clearly shows the presence of quantum scar states with low $S_{L/2}$ separated from the usual thermal states with higher $S_{L/2}$; the circled states are the ones with high overlap with $|\psi(mT)\rangle$. (c) Same as in (a) but for $\hbar\omega_D/Q_0 = 1.25$ displaying ETH obeying rapid thermalization. (d) Same as in (b) but with $\hbar\omega_D/Q_0 = 1.25$. The plot indicates the absence of scars. For (a) and (c), $L = 24$ while for (b) and (d) $L = 18$. For all the plots, all states are chosen from the $W_\ell = 1$ sector, $Q_0/J = 40$, and all energies are scaled with J .

and it shows a violation of ETH in finite-sized chains.

B. Fidelity

In this section, we compute the fidelity

$$\mathcal{F}(mT) = |\langle \psi(mT) | \psi(0) \rangle| \quad (41)$$

starting from the initial state $|\psi(0)\rangle = |\psi_1\rangle$. We begin with the sector with all $W_\ell = 1$. The dimension of this sector scales as $[(\sqrt{5} + 1)/2]^L$ which indicates that the model has the same HSD as the PXP chain. Indeed, it has been shown that the $W_\ell = 1$ sector of the model hosts quantum scars that have a large overlap with $|\psi_1\rangle$; the state $|\psi_1\rangle$ can be mapped to the Neel state of the PXP model using the transformation $|\dots y_j x_{j+1} \dots\rangle \rightarrow |\dots \uparrow_\ell \dots\rangle$ and $|\dots x_j y_{j+1} \dots\rangle \rightarrow |\dots \downarrow_\ell \dots\rangle$, where ℓ denotes the link between the sites j and $j + 1$ [97].

A plot of $\mathcal{F}(mT)$ as a function of m , shown in Fig. 7(a) for $\hbar\omega_D/Q_0 = 5$, shows an oscillatory behavior with distinct revivals; the amplitude of these oscillations decreases in time. This behavior constitutes a clear violation of ETH and can be attributed to quantum scars hosted by $H_F^{(1)}$. The presence of such scars can be understood by noting that for $\hbar\omega_d \gg Q_0$, H_a , H_b and

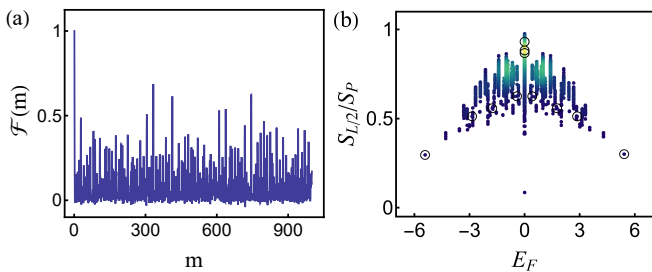


FIG. 8. (a) Plot of $\mathcal{F}(mT)$ as a function of m for $\omega_D = \omega_1^* = Q_0/(2\hbar)$ and $L = 24$ showing strong finite-size fluctuations. (b) Plot of $S_{L/2}/S_p$ for all Floquet eigenstates for $L = 18$ as a function of their quasienergy E_F/J at $\omega_D = \omega_1^*$. For both plots, all states are chosen from the $W_\ell = 1$ sector, $Q_0/J = 40$, and all energies are scaled with J .

H_c have almost the same amplitudes (Eq. 26); consequently, $H_F^{(1)} \simeq H_1$ which is known to host such scars [97]. These scars, which have a large overlap with the state $|\psi(mT)\rangle$, can be clearly seen in Fig. 7(b). In contrast, at $\hbar\omega_D/Q_0 = 1.25$, $\mathcal{F}(mT)$ shows a quick thermalization consistent with ETH as seen in Fig. 7(c); concomitantly, a plot of S/S_p as a function of the energy E_F/J (Fig. 7(d)) shows that $H_F^{(1)}$ does not host scars for this drive frequency. This can be understood by noting that at this frequency, the amplitudes H_a , H_b and H_c are not identical; consequently, $H_F^{(1)}$ is not close to H_1 and it does not host quantum scars. Thus a reduction of the drive frequency at a fixed Q_0 (or equivalently increasing Q_0/ω_D), leads to a crossover from a scar-dominated oscillatory behavior to ETH obeying rapid thermalization of the fidelity.

Upon lowering ω_D further, we reach ω_1^* for which $H_F^{(1)} = H_a$ and the corresponding Hilbert space is strongly fragmented. Here the fidelity depends on the initial state; our choice of $|\psi(0)\rangle = |\psi_1\rangle$ ensures that we address fidelity in the largest fragment. Since this fragment is ergodic, we find rapid thermalization. However, in this case, the HSD of the sector is much smaller compared to the total HSD leading to stronger finite-size effects as can be seen in Fig. 8(a). The fragmented structure of the states can be inferred from Fig. 8(b) which shows a plot of S/S_p for all Floquet eigenstates as a function of their quasienergies E_F/J . The approximately fragmented structure of the Hilbert space can be inferred from the presence of a larger number of zero energy states; we have numerically verified that many of these have large overlaps with Fock states which indicates the presence of near frozen states in the spectrum. We note that the fragmentation here is approximate due to the presence of small but non-zero higher order terms in the Floquet Hamiltonian that do not support HSF.

Finally, we consider the fidelity in the $W_\ell = \{\dots, 1, 1, -1, \dots\}$ sector. Here for $\hbar\omega_D = Q_0/(2n)$, the behavior of $\mathcal{F}(mT)$ is qualitatively similar to the $W_\ell = 1$ sector. For $\hbar\omega_D \gg Q_0$, $H_F^{(1)} \rightarrow H_1$ and consequently

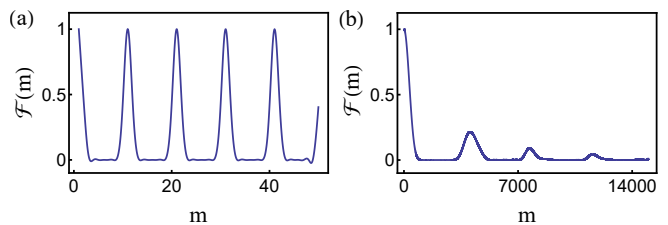


FIG. 9. (a) Plot of $\mathcal{F}(mT)$ starting from the initial state $|\psi_1'\rangle$ as a function of the number of drive cycles m for $\omega_D = \omega_1^* = Q_0/(2\hbar)$ shows an oscillatory behavior with repeated revivals. (b) Same plot but with initial state $|\psi_2'\rangle$ shows thermalization. For both plots, $L = 24$, all initial states are chosen from the $W_\ell = \{\dots, 1, 1, -1, \dots\}$ sector, $Q_0/J = 40$, and all energies are scaled with J .

$\mathcal{F}(mT)$ exhibits scar-induced oscillations similar to that in Fig. 7(a). As $\hbar\omega_D$ is lowered, we find rapid thermalization as seen in Fig. 7(c).

However, the behavior of $\mathcal{F}(mT)$ at the special drive frequency $\omega_D = \omega_1^*$ is qualitatively different from its counterpart for the $W_\ell = 1$ sector. This is shown in Fig. 9. For the initial state $|\psi_1'\rangle$, the first-order Floquet Hamiltonian can be thought as $L/3$ decoupled systems given by Eq. 35 each of which has two states with a quasienergy difference $2J$; consequently, $\mathcal{F}(mT)$ shows periodic revivals after $m^* = \text{Int}(\pi/JT)$. For the parameters used for Fig. 9(a), we find $\hbar\omega_D = 20J$ which predicts $m^* \sim 10$; this matches the numerical result shown quite well.

In contrast, for $|\psi(0)\rangle = |\psi_2'\rangle$ which is a frozen state of $H_F^{(1)}$, we find $\mathcal{F}(mT)$ displays slow dynamics as shown in Fig. 9(b). The deviation of $\mathcal{F}(mT)$ from its initial value in this case occurs solely due to higher order terms in the Floquet Hamiltonian which is non-integrable. Thus $\mathcal{F}(mT)$ eventually reaches its ETH predicted thermal value $\simeq 0$; however, the thermalization is extremely slow since these higher order terms have small amplitudes for $Q_0/J \gg 1$. Such slow thermalization is a consequence of the slow dynamics of a frozen state due to higher-order terms in the Floquet Hamiltonian.

C. Correlation functions

In this section, we study the equal-time correlation function

$$C_{j,j+n}(mT) \equiv C_0 = \langle \psi(mT) | \hat{O}_j \hat{O}_{j+n} | \psi(mT) \rangle, \\ \hat{O}_j = (S_j^x S_{j+1}^y)^2, \quad (42)$$

as a function of m for several drive frequencies. In what follows, we concentrate on C_{24} for the $W_\ell = 1$ sector and C_{25} for the $W_\ell = \{\dots, 1, 1, -1, \dots\}$ sector; our numerical results shown in Fig. 10 shows qualitatively similar behaviors of these correlators in both sectors.

For both sectors at large drive frequencies $\hbar\omega_D \gg Q_0$, $H_F^{(1)} \sim H_0$; hence it supports quantum scars. For initial

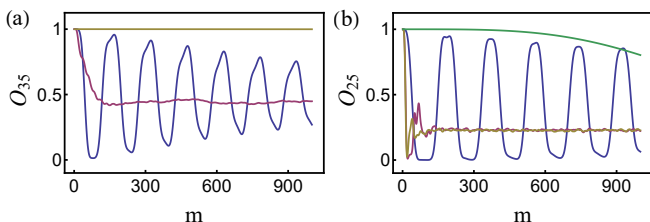


FIG. 10. (a) Plot of C_{24} starting from the initial state $|\psi_1\rangle$ in the $W_\ell = 1$ sector as a function of the number of drive cycles m for $\hbar\omega_D = 5Q_0$ (blue), Q_0 (magenta) and $Q_0/2$ showing scar-induced oscillations, ETH predicted thermalization, and near-constant behavior. (b) Plot of C_{25} with initial state $|\psi'_1\rangle$ in the $W_\ell = \{\dots 1, 1, -1 \dots\}$ sector and with the same color scheme as in (a). For both plots, $L = 24$, $Q_0/J = 40$, and all energies are scaled with J .

states, such as $|\psi_1\rangle$ in the $W_\ell = 1$ sector and $|\psi'_1\rangle$ in the $W_\ell = \{\dots 1, 1, -1 \dots\}$ sector, which have large overlaps with the scar states, C_0 shows oscillatory dynamics. This is shown in Figs. 10 (a) and (b) for $\hbar\omega_D = 5Q_0$ (blue solid lines). Upon reducing the frequencies to $\hbar\omega_D = Q_0$, one sees a ETH predicted thermalization as shown in magenta lines in both panels. The intermediate region shows a gradual crossover between the oscillatory and the thermal behavior and a monotonic reduction in the thermalization time.

At the special frequency $\hbar\omega_D = Q_0/2$, both the sectors show almost constant values of C_0 till a very large value of m . To understand this behavior we consider each sector separately. For the $W_\ell = 1$ sector, for $\hbar\omega_D = Q_0/2$, we have $H_F^{(1)} = H_a$. It can be straightforwardly checked, using Eqs. 24, that H_a connects a state with $|\dots x_{j-1}y_jx_{j+1}y_{j+2}x_{j+3}\dots\rangle$ to $|\dots x_{j-1}z_jz_{j+1}y_{j+2}x_{j+3}\dots\rangle$. Both these states are eigenstates of the operators $\hat{O}_j\hat{O}_{j+2}$. This indicates that $C_{j,j+2}$ for a fixed j and $n = 2$ will be pinned to its initial value. For the $W_\ell = \{\dots 1, 1, -1 \dots\}$ sector, one finds from Eq. 31 that H'_a annihilates the initial state and the dynamics is completely frozen. Thus C_{25} stays close to its original value. The slow deviation of C_{25} from its initial value in the present case is a consequence of higher-order terms in the Floquet Hamiltonian.

V. DISCUSSION

In this work, we have analyzed the dynamics of a periodically driven spin-one chain. The model used is the well-known Kitaev model in one dimension. The key property of the model which makes this analysis possible is the presence of Z_2 -valued conserved quantities, W_ℓ , on every link ℓ of the chain. This fragments the Hilbert space of the spin-chain into sectors labeled by specific values of W_ℓ on each link ℓ . The dimension of the largest (all $W_\ell = 1$) and the second-largest ($W_\ell = \{\dots 1, 1, -1 \dots\}$) sectors are much smaller than the total HSD; this allows

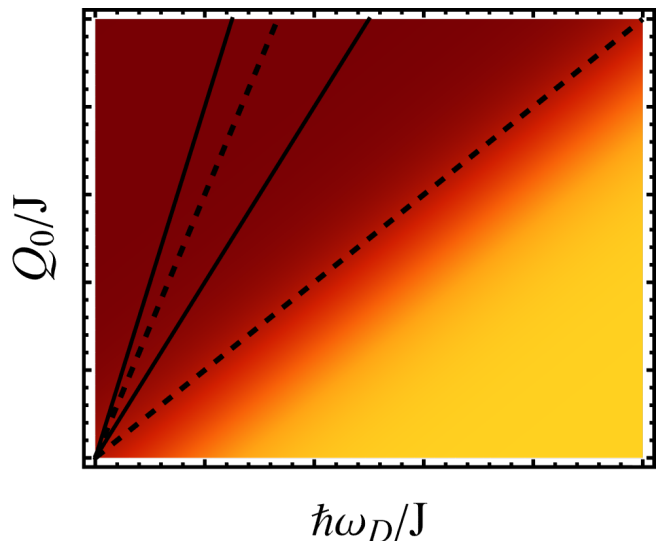


FIG. 11. Schematic phase diagram for the driven spin chain in the $Q_0 - \omega_D$ plane. The yellow region shows scar-induced oscillations while the red region represents Floquet ETH predicted thermalization. Lowering ω_D leads to a gradual crossover between the two regions. The dotted lines correspond to $\hbar\omega_D = Q_0/(2n + 1)$ (where $n = 0, 1, 2, \dots$); they are present only for the sector with all $W_\ell = 1$ and represents weak HSF. They have no analogs in the $W_\ell = \{\dots 1, 1, -1 \dots\}$ sector. The solid lines at $\hbar\omega_D = Q_0/(2n)$ (where $n = 1, 2, 3, \dots$) represent strong HSF for both sectors. See text for details.

one to carry out ED on a finite-sized chain with $L \leq 24$.

We combine exact numerical results from such ED with analytical, perturbative, FPT-based calculation of the first-order Floquet Hamiltonian $H_F^{(1)}$ in the large drive amplitude regime to obtain our results. These are summarized in the schematic phase diagram shown in Fig. 11. For large $\hbar\omega_D/Q_0$, $H_F^{(1)}$ hosts quantum scars for both sectors. For the sector with all $W_\ell = 1$, such scars are the same as those found for the PXP model; in both sectors, such scars lead to oscillatory dynamics of the fidelity and correlation functions. Upon reducing the drive frequency, such scar-induced dynamics is replaced by rapid, ETH predicted, thermalization in both sectors. This is shown schematically in Fig. 11 as a crossover between yellow and red regions. For $\hbar\omega_D = Q_0/(2n + 1)$, one finds a weak HSF for $W_\ell = 1$. The number of Hilbert space fragments grows with the system size but not exponentially. This is shown by dotted lines in Fig. 11. For the $W_\ell = \{\dots 1, 1, -1 \dots\}$ sector, no fragmentation occurs at these frequencies.

For $\hbar\omega_D = Q_0/(2n)$, we find strong HSF for both sectors. For the sector with all $W_\ell = 1$, the largest fragment is ergodic while for the $W_\ell = \{\dots 1, 1, -1 \dots\}$ sector, it is integrable. The presence of such fragmentation is most easily verified by a numerical computation of the half-chain entanglement $S(mT)$ for the $W_\ell = 1$ sector; for large m , S saturates to different values depending on the

initial state. This feature shows violation of ETH and provides a clear indication of the fragmented structure of the Hilbert space. The integrable nature of the largest fragment in the $W_\ell = \{\dots 1, 1, -1 \dots\}$ sector shows up in an oscillatory behavior of S (between the extremal values $S = 0$ and $S = \ln 2$) for an initial state which belongs to this fragment. In addition, \mathcal{F} shows perfect revivals for states in this fragment. These results provide concrete support to the analytic effective decoupled spin-half Hamiltonian (Eq. 35) obtained for this fragment. Furthermore, the correlation functions shows extremely slow dynamics at these frequencies for both sectors. Our numerical results, for both sectors, provide support to the analytic Floquet Hamiltonian obtained using FPT.

To conclude, we have studied the Floquet dynamics of a spin-one chain using both FPT and ED. Our analy-

sis based on this indicates the presence of a rich phase diagram for such dynamics supporting scar-induced oscillations, ETH predicted thermalization, and strong and weak HSF in different regimes of the drive frequency and amplitude. Our study opens up the possibility of studying random and quasiperiodic dynamics of the model which we leave as a subject of future study.

VI. ACKNOWLEDGMENTS

K.S. thanks DST, India for support through the project JCB/2021/000030. D.S. thanks SERB, India for support through the project JBR/2920/000043.

-
- [1] J. Dziarmaga, Dynamics of a quantum phase transition and relaxation to a steady state, *Advances in Physics* **59**, 1063–1189 (2010).
 - [2] A. Polkovnikov, K. Sengupta, A. Silva, and M. Vengalattore, Colloquium: Nonequilibrium dynamics of closed interacting quantum systems, *Rev. Mod. Phys.* **83**, 863 (2011).
 - [3] A. Dutta, G. Aeppli, B. K. Chakrabarti, U. Divakaran, T. F. Rosenbaum, and D. Sen, *Quantum Phase Transitions in Transverse Field Spin Models: From Statistical Physics to Quantum Information* (Cambridge University Press, Cambridge, 2015).
 - [4] A. Chandra, A. Das, and B. Chakrabarti, *Quantum Quenching, Annealing and Computation* (Springer Berlin Heidelberg, 2010).
 - [5] M. Bukov, L. D'Alessio, and A. Polkovnikov, Universal high-frequency behavior of periodically driven systems: from dynamical stabilization to Floquet engineering, *Advances in Physics* **64**, 139 (2015), <https://doi.org/10.1080/00018732.2015.1055918>.
 - [6] L. D'Alessio and A. Polkovnikov, Many-body energy localization transition in periodically driven systems, *Annals of Physics* **333**, 19 (2013).
 - [7] L. D'Alessio, Y. Kafri, A. Polkovnikov, and M. Rigol, From quantum chaos and eigenstate thermalization to statistical mechanics and thermodynamics, *Advances in Physics* **65**, 239 (2016), <https://doi.org/10.1080/00018732.2016.1198134>.
 - [8] S. Shevchenko, S. Ashhab, and F. Nori, Landau-Zener-Stückelberg interferometry, *Physics Reports* **492**, 1 (2010).
 - [9] T. Oka and S. Kitamura, Floquet engineering of quantum materials, *Annual Review of Condensed Matter Physics* **10**, 387–408 (2019).
 - [10] S. Blanes, F. Casas, J. Oteo, and J. Ros, The Magnus expansion and some of its applications, *Physics Reports* **470**, 151–238 (2009).
 - [11] A. Eckardt, Colloquium: Atomic quantum gases in periodically driven optical lattices, *Rev. Mod. Phys.* **89**, 011004 (2017).
 - [12] A. Sen, D. Sen, and K. Sengupta, Analytic approaches to periodically driven closed quantum systems: methods and applications, *Journal of Physics: Condensed Matter* **33**, 443003 (2021).
 - [13] I. Bloch, J. Dalibard, and W. Zwerger, Many-body physics with ultracold gases, *Rev. Mod. Phys.* **80**, 885 (2008).
 - [14] L. Tarruell and L. Sanchez-Palencia, Quantum simulation of the Hubbard model with ultracold fermions in optical lattices, *Comptes Rendus. Physique* **19**, 365–393 (2018).
 - [15] W. W. Ho, T. Mori, D. A. Abanin, and E. G. Dalla Torre, Quantum and classical floquet prethermalization, *Annals of Physics* **454**, 169297 (2023).
 - [16] T. Mori, T. N. Ikeda, E. Kaminishi, and M. Ueda, Thermalization and prethermalization in isolated quantum systems: a theoretical overview, *Journal of Physics B* **51**, 112001 (2018).
 - [17] T. Banerjee and K. Sengupta, Emergent symmetries in prethermal phases of periodically driven quantum systems, *Journal of Physics: Condensed Matter* **37**, 133002 (2025).
 - [18] W. S. Bakr, J. I. Gillen, A. Peng, S. Fölling, and M. Greiner, A quantum gas microscope for detecting single atoms in a Hubbard-regime optical lattice, *Nature* **462**, 74 (2009).
 - [19] W. S. Bakr, A. Peng, M. E. Tai, R. Ma, J. Simon, J. I. Gillen, S. Fölling, L. Pollet, and M. Greiner, Probing the superfluid-to-Mott insulator transition at the single-atom level, *Science* **329**, 547 (2010).
 - [20] H. Bernien, S. Schwartz, A. Keesling, H. Levine, A. Omran, H. Pichler, S. Choi, A. S. Zibrov, M. Endres, M. Greiner, V. Vuletić, and M. D. Lukin, Probing many-body dynamics on a 51-atom quantum simulator, *Nature* **551**, 579 (2017).
 - [21] H. Levine, A. Keesling, A. Omran, H. Bernien, S. Schwartz, A. S. Zibrov, M. Endres, M. Greiner, V. Vuletić, and M. D. Lukin, High-fidelity control and entanglement of Rydberg-atom qubits, *Phys. Rev. Lett.* **121**, 123603 (2018).
 - [22] D. Bluvstein, A. Omran, H. Levine, A. Keesling, G. Semeghini, S. Ebadi, T. T. Wang, A. A. Michailidis, N. Maskara, W. W. Ho, S. Choi, M. Serbyn, M. Greiner, V. Vuletić, and M. D. Lukin, Controlling quantum

- many-body dynamics in driven Rydberg atom arrays, *Science* **371**, 1355 (2021).
- [23] T. Manovitz, S. H. Li, S. Ebadi, R. Samajdar, A. A. Geim, S. J. Evered, D. Bluvstein, H. Zhou, N. U. Koyluoglu, J. Feldmeier, P. E. Dolgirev, N. Maskara, M. Kalinowski, S. Sachdev, D. A. Huse, M. Greiner, V. Vuletić, and M. D. Lukin, Quantum coarsening and collective dynamics on a programmable simulator, *Nature* **638**, 86 (2025).
- [24] X. Liang, Z. Yue, Y.-X. Chao, Z.-X. Hua, Y. Lin, M. K. Tey, and L. You, Observation of anomalous information scrambling in a Rydberg atom array, *Phys. Rev. Lett.* **135**, 050201 (2025).
- [25] Y. Baum, E. van Nieuwenburg, and G. Refael, From dynamical localization to bunching in interacting floquet systems, *SciPost Physics* **5**, 10.21468/scipostphys.5.2.017 (2018).
- [26] D. J. Luitz, Y. Bar Lev, and A. Lazarides, Absence of dynamical localization in interacting driven systems, *SciPost Physics* **3**, 10.21468/scipostphys.3.4.029 (2017).
- [27] A. Agarwala and D. Sen, Effects of interactions on periodically driven dynamically localized systems, *Phys. Rev. B* **95**, 014305 (2017).
- [28] S. Aditya and D. Sen, Dynamical localization and slow thermalization in a class of disorder-free periodically driven one-dimensional interacting systems, *SciPost Phys. Core* **6**, 083 (2023).
- [29] T. Nag, S. Roy, A. Dutta, and D. Sen, Dynamical localization in a chain of hard core bosons under periodic driving, *Phys. Rev. B* **89**, 165425 (2014).
- [30] L. Tamang, T. Nag, and T. Biswas, Floquet engineering of low-energy dispersions and dynamical localization in a periodically kicked three-band system, *Phys. Rev. B* **104**, 174308 (2021).
- [31] M. Fava, R. Fazio, and A. Russomanno, Many-body dynamical localization in the kicked Bose-Hubbard chain, *Phys. Rev. B* **101**, 064302 (2020).
- [32] M. Heyl, A. Polkovnikov, and S. Kehrein, Dynamical quantum phase transitions in the transverse-field ising model, *Phys. Rev. Lett.* **110**, 135704 (2013).
- [33] S. Bandyopadhyay, A. Polkovnikov, and A. Dutta, Observing dynamical quantum phase transitions through quasilocal string operators, *Phys. Rev. Lett.* **126**, 200602 (2021).
- [34] S. Bhattacharjee and A. Dutta, Dynamical quantum phase transitions in extended transverse ising models, *Phys. Rev. B* **97**, 134306 (2018).
- [35] M. Heyl, Dynamical quantum phase transitions: a review, *Reports on Progress in Physics* **81**, 054001 (2018).
- [36] A. Sen, S. Nandy, and K. Sengupta, Entanglement generation in periodically driven integrable systems: Dynamical phase transitions and steady state, *Phys. Rev. B* **94**, 214301 (2016).
- [37] S. Aditya, S. Samanta, A. Sen, K. Sengupta, and D. Sen, Dynamical relaxation of correlators in periodically driven integrable quantum systems, *Phys. Rev. B* **105**, 104303 (2022).
- [38] S. Nandy, K. Sengupta, and A. Sen, Periodically driven integrable systems with long-range pair potentials, *Journal of Physics A* **51**, 334002 (2018).
- [39] A. A. Makki, S. Bandyopadhyay, S. Maity, and A. Dutta, Dynamical crossover behavior in the relaxation of quenched quantum many-body systems, *Phys. Rev. B* **105**, 054301 (2022).
- [40] A. Das, Exotic freezing of response in a quantum many-body system, *Phys. Rev. B* **82**, 172402 (2010).
- [41] S. S. Hegde, H. Katiyar, T. S. Mahesh, and A. Das, Freezing a quantum magnet by repeated quantum interference: An experimental realization, *Phys. Rev. B* **90**, 174407 (2014).
- [42] S. Mondal, D. Pekker, and K. Sengupta, Dynamics-induced freezing of strongly correlated ultracold bosons, *EPL (Europhysics Letters)* **100**, 60007 (2012).
- [43] H. Guo, R. Mukherjee, and D. Chowdhury, Dynamical freezing in exactly solvable models of driven chaotic quantum dots, *Phys. Rev. Lett.* **134**, 10.1103/ggk3-6cf8 (2025).
- [44] U. Divakaran and K. Sengupta, Dynamic freezing and defect suppression in the tilted one-dimensional Bose-Hubbard model, *Phys. Rev. B* **90**, 184303 (2014).
- [45] A. Haldar, D. Sen, R. Moessner, and A. Das, Dynamical freezing and scar points in strongly driven Floquet matter: Resonance vs emergent conservation laws, *Phys. Rev. X* **11**, 021008 (2021).
- [46] N. Gangopadhyay and S. Choudhury, Counterdiabatic route to entanglement steering and dynamical freezing in the Floquet lipkin-meshkov-glick model, *Phys. Rev. Lett.* **135**, 020407 (2025).
- [47] N. Y. Yao and C. Nayak, Time crystals in periodically driven systems, *Physics Today* **71**, 40–47 (2018).
- [48] V. Khemani, R. Moessner, and S. L. Sondhi, A brief history of time crystals (2019), arXiv:1910.10745 [cond-mat.str-el].
- [49] D. V. Else, C. Monroe, C. Nayak, and N. Y. Yao, Discrete time crystals, *Annual Review of Condensed Matter Physics* **11**, 467–499 (2020).
- [50] M. P. Zaletel, M. Lukin, C. Monroe, C. Nayak, F. Wilczek, and N. Y. Yao, Colloquium : Quantum and classical discrete time crystals, *Rev. Mod. Phys.* **95**, 031001 (2023).
- [51] K. Sacha and J. Zakrzewski, Time crystals: a review, *Reports on Progress in Physics* **81**, 016401 (2017).
- [52] C. W. von Keyserlingk, V. Khemani, and S. L. Sondhi, Absolute stability and spatiotemporal long-range order in Floquet systems, *Phys. Rev. B* **94**, 085112 (2016).
- [53] R. Moessner and S. L. Sondhi, Equilibration and order in quantum Floquet matter, *Nature Physics* **13**, 424 (2017).
- [54] D. V. Else, B. Bauer, and C. Nayak, Floquet time crystals, *Phys. Rev. Lett.* **117**, 090402 (2016).
- [55] D. V. Else, B. Bauer, and C. Nayak, Prethermal phases of matter protected by time-translation symmetry, *Phys. Rev. X* **7**, 011026 (2017).
- [56] N. Y. Yao, A. C. Potter, I.-D. Potirniche, and A. Vishwanath, Discrete time crystals: Rigidity, criticality, and realizations, *Phys. Rev. Lett.* **118**, 030401 (2017).
- [57] T. Kitagawa, E. Berg, M. Rudner, and E. Demler, Topological characterization of periodically driven quantum systems, *Phys. Rev. B* **82**, 235114 (2010).
- [58] N. H. Lindner, G. Refael, and V. Galitski, Floquet topological insulator in semiconductor quantum wells, *Nature Physics* **7**, 490 (2011).
- [59] T. Kitagawa, T. Oka, A. Brataas, L. Fu, and E. Demler, Transport properties of nonequilibrium systems under the application of light: Photoinduced quantum hall insulators without landau levels, *Phys. Rev. B* **84**, 235108 (2011).

- [60] M. Thakurathi, A. A. Patel, D. Sen, and A. Dutta, Floquet generation of majorana end modes and topological invariants, *Phys. Rev. B* **88**, 155133 (2013).
- [61] A. Kundu, H. A. Fertig, and B. Seradjeh, Effective theory of Floquet topological transitions, *Phys. Rev. Lett.* **113**, 236803 (2014).
- [62] F. Nathan and M. S. Rudner, Topological singularities and the general classification of Floquet–Bloch systems, *New Journal of Physics* **17**, 125014 (2015).
- [63] B. Mukherjee, A. Sen, D. Sen, and K. Sengupta, Signatures and conditions for phase band crossings in periodically driven integrable systems, *Phys. Rev. B* **94**, 155122 (2016).
- [64] B. Mukherjee, P. Mohan, D. Sen, and K. Sengupta, Low-frequency phase diagram of irradiated graphene and a periodically driven spin- $\frac{1}{2}$ XY chain, *Phys. Rev. B* **97**, 205415 (2018).
- [65] B. Mukherjee, Floquet topological transition by unpolarized light, *Phys. Rev. B* **98**, 235112 (2018).
- [66] S. Pai and M. Pretko, Dynamical scar states in driven fracton systems, *Phys. Rev. Lett.* **123**, 136401 (2019).
- [67] B. Mukherjee, S. Nandy, A. Sen, D. Sen, and K. Sengupta, Collapse and revival of quantum many-body scars via Floquet engineering, *Phys. Rev. B* **101**, 245107 (2020).
- [68] K. Mizuta, K. Takasan, and N. Kawakami, Exact Floquet quantum many-body scars under Rydberg blockade, *Phys. Rev. Res.* **2**, 033284 (2020).
- [69] S. Sugiura, T. Kuwahara, and K. Saito, Many-body scar state intrinsic to periodically driven system, *Phys. Rev. Res.* **3**, L012010 (2021).
- [70] B. Mukherjee, A. Sen, D. Sen, and K. Sengupta, Dynamics of the vacuum state in a periodically driven Rydberg chain, *Phys. Rev. B* **102**, 075123 (2020).
- [71] N. Maskara, A. A. Michailidis, W. W. Ho, D. Bluvstein, S. Choi, M. D. Lukin, and M. Serbyn, Discrete time-crystalline order enabled by quantum many-body scars: Entanglement steering via periodic driving, *Phys. Rev. Lett.* **127**, 090602 (2021).
- [72] A. Hudomal, J.-Y. Desaulles, B. Mukherjee, G.-X. Su, J. C. Halimeh, and Z. Papić, Driving quantum many-body scars in the pxp model, *Phys. Rev. B* **106**, 104302 (2022).
- [73] B. Huang, T.-H. Leung, D. M. Stamper-Kurn, and W. V. Liu, Discrete time crystals enforced by Floquet–Bloch scars, *Phys. Rev. Lett.* **129**, 133001 (2022).
- [74] P. Sala, T. Rakovszky, R. Verresen, M. Knap, and F. Pollmann, Ergodicity breaking arising from Hilbert space fragmentation in dipole-conserving hamiltonians, *Phys. Rev. X* **10**, 011047 (2020).
- [75] V. Khemani, M. Hermele, and R. Nandkishore, Localization from Hilbert space shattering: From theory to physical realizations, *Phys. Rev. B* **101**, 174204 (2020).
- [76] S. Moudgalya, B. A. Bernevig, and N. Regnault, Quantum many-body scars and Hilbert space fragmentation: a review of exact results, *Reports on Progress in Physics* **85**, 086501 (2022).
- [77] S. Ghosh, I. Paul, and K. Sengupta, Prethermal fragmentation in a periodically driven fermionic chain, *Phys. Rev. Lett.* **130**, 120401 (2023).
- [78] S. Ghosh, I. Paul, and K. Sengupta, Signatures of fragmentation for periodically driven fermions, *Phys. Rev. B* **109**, 214304 (2024).
- [79] C. M. Langlett and S. Xu, Hilbert space fragmentation and exact scars of generalized Fredkin spin chains, *Phys. Rev. B* **103**, L220304 (2021).
- [80] L. Zhang, Y. Ke, L. Lin, and C. Lee, Floquet engineering of Hilbert space fragmentation in Stark lattices, *Phys. Rev. B* **109**, 184313 (2024).
- [81] S. Ghosh, I. Paul, K. Sengupta, and L. Vidmar, Destructive interference induced constraints in Floquet systems (2025), arXiv:2508.18368 [cond-mat.str-el].
- [82] S. Ghosh, I. Paul, and K. Sengupta, Signatures of fragmentation for periodically driven fermions, *Phys. Rev. B* **109**, 214304 (2024).
- [83] S. Aditya, D. Dhar, and D. Sen, Subspace-restricted thermalization in a correlated-hopping model with strong Hilbert space fragmentation characterized by irreducible strings, *Phys. Rev. B* **110**, 045418 (2024).
- [84] M. Ganguli, S. Aditya, and D. Sen, Aspects of Hilbert space fragmentation in the quantum East model: Fragmentation, subspace-restricted quantum scars, and effects of density-density interactions, *Phys. Rev. B* **111**, 045411 (2025).
- [85] B. Paul, T. Mishra, and K. Sengupta, Floquet realization of prethermal Meissner phase in a two-leg flux ladder (2025), arXiv:2504.11017 [cond-mat.quant-gas].
- [86] M. V. Berry, Transitionless quantum driving, *Journal of Physics A* **42**, 365303 (2009).
- [87] A. del Campo and K. Sengupta, Controlling quantum critical dynamics of isolated systems, *The European Physical Journal Special Topics* **224**, 189 (2015).
- [88] T. Banerjee, S. Choudhury, and K. Sengupta, Exact Floquet flat band and heating suppression via two-tone drive protocols, *New Journal of Physics* **27**, 084506 (2025).
- [89] T. Mori, T. Kuwahara, and K. Saito, Rigorous bound on energy absorption and generic relaxation in periodically driven quantum systems, *Phys. Rev. Lett.* **116**, 120401 (2016).
- [90] T. Kuwahara, T. Mori, and K. Saito, Floquet–Magnus theory and generic transient dynamics in periodically driven many-body quantum systems, *Annals of Physics* **367**, 96 (2016).
- [91] D. Abanin, W. De Roeck, W. W. Ho, and F. Huveneers, A rigorous theory of many-body prethermalization for periodically driven and closed quantum systems, *Communications in Mathematical Physics* **354**, 809 (2017).
- [92] D. A. Abanin, W. De Roeck, W. W. Ho, and F. m. c. Huveneers, Effective hamiltonians, prethermalization, and slow energy absorption in periodically driven many-body systems, *Phys. Rev. B* **95**, 014112 (2017).
- [93] N. O’Dea, F. Burnell, A. Chandran, and V. Khemani, Prethermal stability of eigenstates under high frequency floquet driving, *Phys. Rev. Lett.* **132**, 100401 (2024).
- [94] D. M. Long, P. J. D. Crowley, V. Khemani, and A. Chandran, Phenomenology of the prethermal many-body localized regime, *Phys. Rev. Lett.* **131**, 106301 (2023).
- [95] R. Mukherjee, H. Guo, and D. Chowdhury, Floquet thermalization via instantons near dynamical freezing, *Phys. Rev. X* **16**, 011041 (2026).
- [96] A. J. Raja and R. Ganesh, The Kitaev-AKLT model (2025), arXiv:2510.12880 [cond-mat.str-el].
- [97] S. Mohapatra and A. C. Balram, Pronounced quantum many-body scars in the one-dimensional spin-1 Kitaev model, *Phys. Rev. B* **107**, 235121 (2023).

- [98] D. Sen, R. Shankar, D. Dhar, and K. Ramola, Spin-1 Kitaev model in one dimension, *Phys. Rev. B* **82**, 195435 (2010).
- [99] P. Fendley, K. Sengupta, and S. Sachdev, Competing density-wave orders in a one-dimensional hard-boson model, *Phys. Rev. B* **69**, 075106 (2004).
- [100] D. N. Page, Average entropy of a subsystem, *Phys. Rev. Lett.* **71**, 1291 (1993).